

Thesis for the Degree of
Master of Science in Civil and Environmental Engineering

**Quantifying Uncertainty in Future Extreme Precipitation
Projections: A Dual Focus on Scaling Rates and Physical Changes**

미래 극한 강수 예측의 불확실성 정량화: 스케일링 속도와 물리
적 변화에 대한 이중 관점



MIN SOTHEARITH
Department of Civil and Environmental Engineering

The Graduate School of
Kongju National University
Republic of Korea

June 2025

**Quantifying Uncertainty in Future Extreme Precipitation
Projections: A Dual Focus on Scaling Rates and Physical Changes**

미래 극한 강수 예측의 불확실성 정량화: 스케일링 속도와 물리
적 변화에 대한 이중 관점

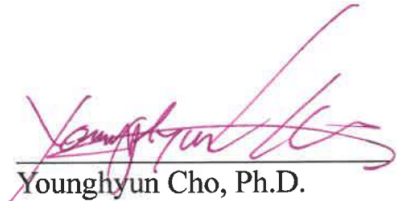
A Thesis presented to the
Department of Civil and Environmental Engineering
The Graduate School of
Kongju National University
Republic of Korea

In Partial Fulfillment of the Requirements
For the Degree of
Master of Science in Civil and Environmental Engineering

By
MIN SOTHEARITH

June 2025

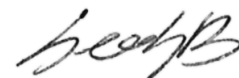
The Thesis for the Degree of Master of Science in Civil and Environmental
Engineering of MIN SOTHEARITH is accepted and approved.



Younghyun Cho
Younghyun Cho, Ph.D.



Kuk-Hyun Ahn
Kuk-Hyun Ahn, Ph.D.



Seung Beom Seo, Ph.D.
Committee Chair

Kongju National University
Republic of Korea

June 2025

Table of Contents

Table of Contents	i
List of Figures.....	iii
List of Tables.....	vii
I. Introduction	1
1. Background	1
2. Research Goals and Objectives.....	6
II. Literature Review	7
1. Global Circulation Models.....	7
2. The Uncertainty of Future Projections	8
III. Study I: Uncertainty Decomposition of Scaling Rates	11
1. Introduction.....	11
2. Objectives	13
3. Data and Methods	14
3.1. Future Emission Scenarios.....	15
3.2. Global Circulation Models (GCMs)	16
3.3. Scaling Methods.....	19
3.4. Sobol' Sensitivity Analysis	21
3.5. Framework for Quantifying Numbers of GCMs.....	22
4. Results	23
4.1. Uncertainty Decomposition of the Projected Scaling Rates	23
4.2. GCM Quantity in the Uncertainty Decomposition Framework	30

4.3. A Comparison Between CMIP5 and CMIP6	37
5. Discussions	47
6. Conclusions of Study I.....	49
IV. Study II: Uncertainty Decomposition of Changes in Extreme Precipitation	51
1. Introduction.....	51
2. Objectives	53
3. Data and Methods	54
3.1. Future Emission Scenarios and GCMs	55
3.2. Physical Diagnostic Model	57
3.3. Uncertainty Decomposition Framework.....	58
3.4. Signal-to-Noise Ratio (<i>SNR</i>)	59
4. Results	60
4.1. Changes of <i>Rx1Day</i> and the Contributions from <i>TH</i> and <i>DY</i> ..	60
4.2. Uncertainty of Changes and the Decomposition.....	64
4.3. <i>SNR</i> Analysis.....	69
5. Discussions	73
6. Conclusions of Study II.....	76
V. Overall Conclusions	79
References.....	82
Abstract*.....	90
국문초록	92
Acknowledgment	94

List of Figures

Figure 1. The overview of the study design.....	15
Figure 2. Geographic distribution of 26 regional areas utilized in this study. The regional definitions are adopted from the IPCC Special Report on Managing the Risks of Extreme Events and Disasters to Advance Climate Adaptation (SREX).....	16
Figure 3. The average of estimated scaling rates and their spread (difference between the 90th and 10th quantile) across 153 ensembles for the entire simulation period (2041-2090): (a) average scaling rates for grids, (b) average scaling rates for regions, (c) spread for grids, and (d) spread for regions.....	25
Figure 4. Global uncertainty contributions from each source: (a) GCMs, (b) future emission scenarios, (c) scaling methods, (d) interaction between GCMs and future emission scenarios, (e) interaction between GCMs and scaling methods, and (f) interaction between future emission scenarios and scaling methods. The values in the box at the bottom left of each panel represent the global average across all grid points.	27
Figure 5. Uncertainty contribution from all sources for six regions: (a) AMZ, (b) CGI, (c) NAS, (d) SSA, (e) SAF, and (f) NAU; along with (g) the global average. In each panel, colors represent the uncertainty contribution from different sources: blue for GCMs, purple for future emission scenarios, red for scaling methods, yellow for interactions between GCMs and future emission scenarios, green for interactions between	

GCMs and scaling methods, and pink for interactions between future emission scenarios and scaling methods.	29
Figure 6. Same as Figure 5, but for the remaining 20 regions.	30
Figure 7. Uncertainty contribution from varying numbers of GCMs, ranging from 2 to 17. (a) Average uncertainty contribution over 31 simulation periods from GCMs of 6 regions that were presented in Figure 4. Each scatter point represents the average values of all possible combination pairs taken from the 17 GCMs. The shaded red line denotes the $\pm 5\%$ of uncertainty contribution from the 17 GCMs, represented by red points.	
(b) Globally averaged uncertainty for each simulation period. The hatch in each cell of the heat map indicates values within $\pm 5\%$ of uncertainty contribution from the 17 GCMs.	32
Figure 8. Same as Figure 7a, but for the remaining 20 regions.	33
Figure 9. Distribution of uncertainty contributions across six regions: (a) AMZ, (b) CGI, (c) NAS, (d) SSA, (e) SAF, and (f) NAU for different numbers of GCMs (2, 5, 9, 10, 12, 14, 16): Each bar represents a sample from combinations within each group of each number of GCM.	35
Figure 10. Same as Figure 9, but for the remaining 20 regions.	36
Figure 11. Same as Figure 3, but for CMIP5.	40
Figure 12. Same as Figure 4, but for CMIP5.	41
Figure 13. The differences of the uncertainty contribution of each source between CMIP6 and CMIP5 (CMIP6-CMIP5). (a) GCMs, (b) future emission scenarios, (c) scaling methods, (d) interaction between GCMs and future emission scenarios, (e) interaction between GCMs and scaling methods,	

and (f) interaction between future emission scenarios and scaling methods. Purple color indicates negative values, where an uncertainty source contributes in CMIP5 more than in CMIP6, while orange indicates the opposite. The values in the box at the bottom left of each panel represent the global average across all grid points. 42

Figure 14. Same as Figure 6, but for 26 regions of CMIP5. 45

Figure 15. Differences in uncertainty contributions between CMIP6 and CMIP5 (CMIP6 - CMIP5). The first column illustrates regional differences, with bars indicating the average across all simulation periods and error bars representing the magnitude of the standard deviation. The second column depicts global averages for each simulation period, with a line plot showing the average value and a shaded red area indicating the magnitude of the standard deviation. 46

Figure 16. Spatial and temporal changes in *Rx1Day* under SSP1-2.6 (a, b), SSP2-4.5 (c, d), and SSP5-8.5 (e, f). Panels (a), (c), and (e) show spatial averages across all years and GCMs for each scenario at each grid point. Panels (b), (d), and (f) display temporal trends, computed as averages over all grids and GCMs for each scenario by year, followed by linear regression. The orange text indicates the p-value of the regression.... 63

Figure 17. Spatial and temporal changes in *TH* and *DY* components under SSP1-2.6 (a, b, c), SSP2-4.5 (d, e, f), and SSP5-8.5 (g, h, i). Panels (a, d, g) and (b, e, h) show spatial averages across all years and GCMs for each scenario at each grid point for *TH* and *DY* respectively. Panels (c), (f), and (i) display temporal trends, computed as averages over all grids and

GCMs for each scenario by year, followed by linear regression. The left-y axis for <i>TH</i> represented purple while the right-y for <i>DY</i> represented orange color. The texts indicate the p-value of the regression.	64
Figure 18. Uncertainty contributions from the three sources for the global average over time (a, c, e), and the corresponding total uncertainties (b, d, f). Panels (a, b) represent <i>Rx1Day</i> changes, (c, d) show its <i>TH</i> component, and (e, f) illustrate the <i>DY</i> component.	67
Figure 19. Global uncertainty contributions from all sources. Each large panel represents <i>Rx1Day</i> changes (first), <i>TH</i> (second), and <i>DY</i> (last). Each column corresponds to a different source of uncertainty, and each row shows a different time slice: Near Future (2021–2040), Mid Future (2051–2070), and Far Future (2081–2100).	68
Figure 20. Spatially distribution of <i>SNR</i> for <i>TH</i> (first column) and <i>DY</i> (second column). Each row shows a different time slice: Near Future (2021–2040), Mid Future (2051–2070), and Far Future (2081–2100).	71
Figure 21. Spatially distribution of how noise in <i>TH</i> (first column) and <i>DY</i> (second column) would affect the signal of <i>Rx1Day</i> changes. Each row shows a different time slice: Near Future (2021–2040), Mid Future (2051–2070), and Far Future (2081–2100).	72

List of Tables

Table 2. Summary of the seventeen CMIP6 GCMs utilized study I.....	18
Table 3. Summary of the ten CMIP5 GCMs utilized in study I.....	37
Table 4. Summary of the twenty CMIP6 GCMs utilized in study II.	56

I. Introduction

1. Background

Disasters such as floods, mudslides, and landslides are often the result of extreme precipitation. These events pose serious threats to both human populations and ecosystems, potentially resulting in consequences such as loss of life, infrastructure damage, economic disruption, soil erosion or tree uprooting (Aldardasawi and Eren, 2021; Garg and Mishra, 2019; Paterson et al., 2018). In 2024 alone, extreme precipitation contributed to over 8,700 deaths, the displacement of 40 million people, and more than \$550 billion in damages (Van Dijk et al., 2024). A review by Green et al. (2025) noted that several of the costliest weather-related disasters on record occurred in 2024, including Hurricane Milton and Hurricane Helene. Hurricane Milton led to the evacuation of seven million people, causing more than 16 fatalities, and leaving three million without power. Hurricane Helene resulted in 227 deaths, nearly two million power outages, and \$35 billion in economic losses. Additionally, a record-breaking European storm, Boris, brought extreme precipitation that caused flash floods and landslides across regions such as Bavaria and Valencia, resulting in around \$13.87 billion damage and 229 fatalities. These events made 2024 the wettest year since 1998, a record consistent with scientific expectations under global warming. As anthropogenic warming intensifies the hydrological cycle and increases atmospheric moisture, extreme precipitation events are becoming

more frequent and severe (IPCC, 2021). In light of these escalating impacts, developing reliable projections of extreme precipitation is critical for strengthening disaster preparedness, guiding adaptation planning, and minimizing future risks in a warming world.

Global Circulation Models (GCMs) have been the primary climate models employed by scientists to access future climate conditions through computational simulation (Eyring et al., 2016). GCMs have been made available through the Coupled Model Intercomparison Project (CMIP) under the World Climate Research Programme (WCRP) in different generations (Sansom et al., 2013). Currently, CMIP is undergoing its sixth phase (CMIP6). CMIP6 integrates Shared Socioeconomic Pathways (SSP) scenarios, which encompass not just greenhouse gas emissions but also socioeconomic factors like population growth, rate of technological development, and many other relevant factors (O'Neill et al., 2016). Nonetheless, the lack of comprehensive understanding regarding future emissions introduces uncertainty in these future emission scenarios (Riahi et al., 2017). Moreover, the diverse model structure of individual GCMs contributes significantly to uncertainty dispersion in future climate projections (Knutti et al., 2019). Natural fluctuations, often referred to as internal variability, also contribute significantly to uncertainty in climate projections (Blanusa et al., 2023; Maher et al., 2021; Miao et al., 2023). These fluctuations stem from differences in the initial conditions used when running the model, which lead to variations in complex atmospheric and oceanic processes that are inherently unpredictable (Liu et al., 2017; Materia et al., 2014; Strobach and Bel, 2017). As a result,

internal variability introduces an additional layer of uncertainty in climate models.

Scientists often aim to utilize as many GCMs as possible, based on the rationale that in the absence of definitive knowledge about the future, a larger ensemble of models better captures the range of plausible outcomes (Jebeile and Crucifix, 2020; Raju and Kumar, 2020). However, employing a large number of GCMs can impose substantial computational burdens. In practice, there may exist a number of GCMs that are sufficient to yield comparable results, making the use of the full ensemble redundant (Braun et al., 2021). As discussed in Wang et al. (2020), identifying such an optimal subset can help balance computational efficiency with representational robustness.

One widely studied perspective on future extreme precipitation changes focuses on its relationship with temperature, commonly known as the scaling rate. According to the Clausius-Clapeyron relation, extreme precipitation is expected to increase by approximately 7% for every 1°C rise in temperature (Allan and Soden, 2008; Fischer and Knutti, 2016). Scaling rates are typically estimated using paired temperature and precipitation data, with various choices of scaling methods such as quantile regression (Wasko and Sharma, 2014), binning methods with equal-width bins (Lenderink and van Meijgaard, 2008), or equal sample size bins (Hardwick Jones et al., 2010). However, the diversity in scaling methods introduces methodological disagreement, making cross-study comparisons challenging and raising questions about the robustness of scaling estimates (Fowler et al., 2021). This introduces an additional layer of uncertainty to future

projections, beyond those already posed by climate models and emission scenarios. However, the extent to which GCMs, emission scenarios, and scaling methods contribute to the overall uncertainty in scaling rates remains largely unquantified. A clearer understanding of these contributions would benefit both future research and policymaking by enhancing confidence in projections of extreme precipitation under climate change.

Another approach to understanding future changes in extreme precipitation is to directly examine the difference between historical and future periods, as demonstrated in numerous studies (Dai et al., 2024; Ghausi et al., 2024; Huang et al., 2023; Li et al., 2025). These studies primarily focus on the actual change in extreme precipitation metrics, such as annual maximum daily precipitation (R_{x1Day}), rather than its statistical relationship with warming. However, such projected changes often exhibit substantial uncertainty (Dai et al., 2024; Li et al., 2025). To better understand the sources of this uncertainty, scientists have sought to unravel the underlying physical mechanisms by decomposing extreme precipitation into two components: dynamic processes, related to atmospheric circulation, and thermodynamic processes, associated with moisture availability and temperature (O’Gorman and Schneider, 2009). Past studies have shown that thermodynamic processes generally lead to a global increase in extreme precipitation, while dynamic processes can contribute to regional decreases (Ritzhaupt and Maraun, 2024; Dai et al., 2024; Paik et al., 2023). A substantial portion of the uncertainty in projected changes has been attributed to dynamic processes at the global scale, whereas thermodynamic uncertainty tends to be

more pronounced in mid- to high-latitude regions (Li et al., 2025). However, to the best of my knowledge, existing studies have only decomposed the total uncertainty in projected changes of extreme precipitation. No study has yet investigated the individual contributions of key uncertainty sources—such as GCM, emission scenario, and internal variability—to the thermodynamic and dynamic components separately.

2. Research Goals and Objectives

Given the critical impacts of extreme precipitation on society, developing reliable future projections is essential. However, these projections often carry substantial uncertainties, making it crucial to understand their underlying sources in order to potentially reduce them. Despite growing attention, the uncertainty associated with extreme precipitation remains insufficiently understood from both statistical and physical perspectives. In the case of scaling rates, there is still a lack of clarity regarding how different scaling methods, GCMs, and emission scenarios individually contribute to overall uncertainty. Additionally, the minimum number of GCMs needed to maintain robust results without computational redundancy has yet to be systematically assessed. On the physical changes side, although some studies have decomposed uncertainty in projected changes of extreme precipitation (e.g., Lafferty and Srivatava, 2023; Zhang and Chen, 2021), the specific contributions of GCMs, scenarios, and internal variability to the dynamic and thermodynamic components remain largely unexplored. This thesis aims to fill key knowledge gaps by conducting a comprehensive assessment of uncertainties in extreme precipitation projections in both angles of extreme precipitation.

II. Literature Review

1. Global Circulation Models

Scientists have long sought to understand the Earth's circulation, with conceptual foundations laid in the early 20th century (e.g., Abbe, 1901; Courant et al., 1928), and the first computational models emerging mid-century with the advent of digital computers (e.g., Charney et al., 1950). Subsequently, during the 1960s, the works of Syukuro Manabe (Manabe and Möller, 1961; Manabe and Strickler, 1964; Manabe and Wetherald, 1967), which earned him the 2021 Nobel Prize in Physics, modeled the impact of greenhouse gases and other climate dynamics on Earth's warming. This contribution significantly advanced both the understanding and modeling of the Earth's climate system. Manabe and Wetherald (1975) later published the first simulation of global warming using a climate model. This breakthrough set the stage for the development of climate models and laid the foundation for the creation of GCMs. Over time, these models have been refined and expanded to better capture the complex interactions within the Earth's system, including coupled atmosphere-ocean-land-sea ice-land ice dynamics (Randall et al., 2018). These GCMs are developed and coordinated through international projects such as the Coupled Model Intercomparison Project (CMIP), which allows scientists to collaborate and deepen their understanding of the Earth. Currently, CMIP is in its sixth phase (CMIP6), with over 100 GCMs available and more than 50 institutes participating in the project globally.

One of the main goals of GCMs is to project future climatic conditions(IPCC, 2021). To achieve this, scenarios describing the future state of the world—such as greenhouse gas emissions, chemically reactive gases, aerosols, and land use changes—are fed into the mathematical models of GCMs (Eom et al., 2013). These scenarios enable the assessment of possible climate system outcomes, helping to guide adaptation and mitigation strategies under a wide range of potential futures (O'Neill et al., 2016). Starting from CMIP3, four SRES scenarios were introduced. A1 imagines fast economic growth and global integration. A2 depicts regional development with high population growth. B1 focuses on global sustainability with clean technology. B2 emphasizes local sustainability with moderate growth (Nakicenovic et al., 2000). Later in CMIP5, scenarios were developed using Representative Concentration Pathways (RCPs). Unlike the SRES scenarios, RCPs are defined by radiative forcing targets (e.g., 2.6, 4.5, 6.0, 8.5 W/m² by 2100) (Taylor et al., 2012). Building on this, CMIP6 introduced a more integrated framework by combining RCPs with Shared Socioeconomic Pathways (SSPs), forming SSP-RCP scenarios (e.g., SSP1-2.6, SSP2-4.5, SSP5-8.5). SSPs represent different socio-economic trajectories, such as sustainability, regional rivalry, or fossil-fueled development (O'Neill et al., 2016).

2. The Uncertainty of Future Projections

Each institute uses different parameterizations in each GCM to represent the Earth's circulation (Eyring et al., 2016), leading to considerable differences in

climate projections. When combined with the unpredictability of future emission scenarios, this results in substantial variation in projected outcomes. Hawkins and Sutton (2009), published a meaningful study on the sources of uncertainty in climate projections, providing a foundational framework for understanding these complexities. According to the aforementioned study, the uncertainty in climate projections can be categorized into three main sources: climate models, future emission scenarios, and internal variability. Internal variability refers to the natural fluctuations in the Earth's climate system that occur without any external radiative forcing (Hawkins and Sutton, 2009). It arises when models are initialized with slightly different starting conditions, leading to divergent evolutions of the climate system over time, such as El Niño–Southern Oscillation (ENSO) or La Niña events (Sun et al., 2018; Maher et al., 2021). It contributes significantly to the variability of important climate variables, including extreme precipitation events (Lafferty and Srivatava, 2023).

Since Hawkins and Sutton (2009), numerous studies have focused on quantifying the contributions of different sources of uncertainty to various climate variables using a range of methodological approaches. Hawkins and Sutton (2009) proposed fitting the ensemble time series with a fourth-order polynomial and attributing the residuals to internal variability. This method will later be referred to as HS09. It has been applied to other variables such as runoff (Miao et al., 2023), drought (Ji et al., 2024), evapotranspiration and soil moisture (Wu et al., 2024). In parallel, other researchers have employed Analysis of Variance (ANOVA) techniques to decompose uncertainties (e.g., Yip et al., 2011; S. Zhang

et al., 2023). Both approaches aim to partition uncertainty into model, scenario, and internal variability components. However, a key distinction lies in their data requirements: the HS09 method requires only a single ensemble member per GCM-scenario pair, making it suitable when not more than one ensemble member is available. ANOVA-based methods, on the other hand, require multiple ensemble members to robustly estimate internal variability, but offer the additional advantage of capturing interactions between sources of uncertainty. More recently, an extension of HS09 by Lehner et al. (2020), hereafter L20, used Single Model Initial-condition Large Ensembles (SMILEs) to decompose uncertainty. While L20 requires fewer GCMs, it relies on a much larger number of ensemble members for each GCM. L20 has shown results comparable to HS09, but it attributes greater contribution to internal variability, as it directly quantifies uncertainty across the entire ensemble rather than inferring it from residuals. Besides that, some studies have also employed alternative decomposition methods, such as Sobol's sensitivity analysis (Steinschneider et al., 2023). Similar to ANOVA, Sobol's sensitivity analysis requires multiple ensemble simulations to account for internal variability. However, unlike ANOVA, Sobol's method can capture non-linear interactions and does not rely on statistical assumptions such as normality or homoscedasticity (Archer et al., 1997).

III. Study I: Uncertainty Decomposition of Scaling Rates

1. Introduction

In the 1830s, a French physicist, Émile Clapeyron (Clapeyron, 1834) proposed a thermodynamic principle that was later refined by German physicist Rudolf Clausius (Clausius, 1850). This principle, now known as the Clausius-Clapeyron relation (CC relation), describes how the saturation vapor pressure of water increases with temperature. According to this relationship, the water-holding capacity of the atmosphere is expected to increase by approximately 7% per 1°C rise in temperature. About 150 years later, as extreme precipitation became a growing concern for scientists, Allen and Ingram (2002) and Trenberth et al. (2003) demonstrated that changes in atmospheric water vapor with warming are closely linked to variations in extreme precipitation.

In subsequent years, numerous studies have investigated scaling rates both regionally and globally, with a focus on understanding extreme precipitation in the context of global warming. Some have relied on historical data (e.g., Ali et al., 2018; Hardwick Jones et al., 2010; Westra et al., 2014), while others have used projected data from climate models (e.g., Gu et al., 2023; John et al., 2022; O’Gorman and Schneider, 2009). However, these studies revealed significant discrepancies in estimated scaling rates compared to the expected CC scaling. Even when using observed data, variations

in estimated scaling rates may arise from differences in statistical modeling methods and regional moisture limitations. However, these variations can potentially be reduced by pooling grid data to increase sample sizes and incorporating dewpoint temperature as a scaling variable (e.g., Ali et al., 2018; Fowler et al., 2021; Martinkova and Kysely, 2020). On the other hand, for the projection studies, the variations of estimated scaling rates are more severe. To be specific, those studies face additional uncertainties from climate model simulation due to variations in climate model structures and future emission scenarios (John et al., 2022; Kharin et al., 2013; Li et al., 2021).

An additional layer of uncertainty in estimating scaling rates arises from the diversity of scaling methods developed, as scientists have chosen different methods in their studies. For instance, Lenderink and van Meijgaard, (2008) introduced the equal bin width binning method, which was also employed by Lenderink et al. (2011), Park and Min (2017) and Wasko and Sharma (2014). This method categorizes precipitation data by temperature into equal-width bins. It then selects a high quantile value (e.g., 95th, 99th, or 99.5th) of precipitation from each bin and the temperature midpoint of each bin as the representative pair. Finally, it fits the temperature-extreme precipitation pairs to a linear model to calculate the scaling rate. By modifying the aforementioned method, Hardwick Jones et al. (2010) binned the precipitation data by temperature with each bin having equal precipitation data distributed. This method has been followed by numerous studies, as seen in Ali et al. (2018), Mishra et al. (2012) and Yoo and Ahn (2023). Selecting a hyperparameter is required before applying both binning methods. For the equal bin width method, the bin width must be specified, with 2°C being a common choice in many studies (Lenderink et al., 2011; Park and Min, 2017; Wasko

and Sharma, 2014). Similarly, for the equal sample sizes method, the number of bins must be determined, with options such as 12, 15, 20, or 30, as seen in various studies (Ali et al., 2018; Mishra et al., 2012; Yoo and Ahn, 2023). However, it is worth noting that Pumo et al. (2019) found that the choice of the number of bins does not significantly impact scaling rate estimations. In addition to binning methods, Wasko and Sharma (2014) proposed the use of quantile regression to detect the relationship between high-quantile precipitation and temperature without having to bin the data first. Subsequently, many studies, such as Molnar et al. (2015) and Schroeer and Kirchengast (2018), also employed quantile regression in their scaling rate estimation. Regardless of the different scaling methods utilized in various studies, comparing different scaling studies proves challenging due to methodological disagreements (Fowler et al., 2021), leading to inherent uncertainty when determining the scaling rate, especially with a small sample size (Ali et al., 2022; Wasko and Sharma, 2014).

2. Objectives

This section aims to quantify the contributions of GCMs, future emission scenarios, and modeling methodologies to the overall uncertainty in estimated scaling rates at the global scale. In addition, we will assess the minimum number of GCMs required to obtain robust and reliable results. A comparative analysis between the Coupled Model Intercomparison Project Phase 5 (CMIP5) and Phase 6 (CMIP6) will also be conducted to evaluate differences in uncertainty decomposition across the two phases, with a particular focus on the relative contributions of each source of uncertainty.

To be specific, we will address four scientific questions:

1. How does each source contribute to the overall uncertainty in scaling rates?
2. How many GCMs are necessary for a robust uncertainty decomposition?
3. What are the differences in uncertainty contributions from each source between CMIP5 and CMIP6?

3. Data and Methods

This study utilized three sources of uncertainty in the scaling rate estimation for future simulations: future emission scenarios, GCMs, and scaling methods (refer to Figure 1). The modeling chain incorporated 3 future emission scenarios, 17 GCMs, and 3 scaling methods, generating an extensive ensemble of projections for the future period from 2041 to 2090. In total, 153 ensembles were utilized in our analysis. The modeling chain was applied individually to each grid and pooled the data from grids for regional scaling. This study adapted the 26 regions from the IPCC Special Report on Managing the Risks of Extreme Events and Disasters to Advance Climate Adaptation (SREX) (Seneviratne et al., 2012) (Figure 2). Subsequently, the Sobol' sensitivity analysis (Sobol', 1990) was employed to determine the uncertainty contribution from each source. Moreover, Sobol' sensitivity analysis was systematically conducted across all possible combinations of GCMs to investigate how the number of GCMs influences their contribution to overall uncertainty quantification.

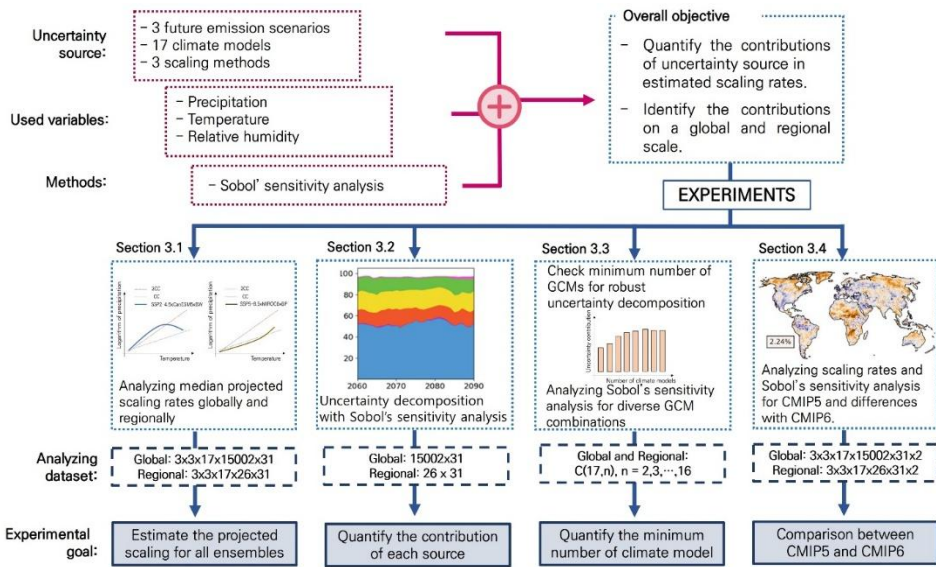


Figure 1. The overview of the study design.

3.1. Future Emission Scenarios

In this study, three future emission scenarios were selected: SSP1-2.6, SSP2-4.5, and SSP5-8.5, which represent low, medium, and high future emission levels, respectively (O'Neill et al., 2016). The SSP1-2.6 scenario represents a sustainability “taking a green road” with a radiative forcing of 2.6 W/m^2 , SSP2-4.5 denotes as a “middle of the road” scenario with a radiative forcing of 4.5 W/m^2 , and SSP5-8.5 portrays an “end of the road” scenario with a radiative forcing of 8.5 W/m^2 (Riahi et al., 2017). These three scenarios encompass a broad range of possible future emissions. Additionally, previous uncertainty decomposition studies, including Lehner et al. (2020), Wu et al. (2024) and Zhang et al. (2023) have also utilized these scenarios in their studies.

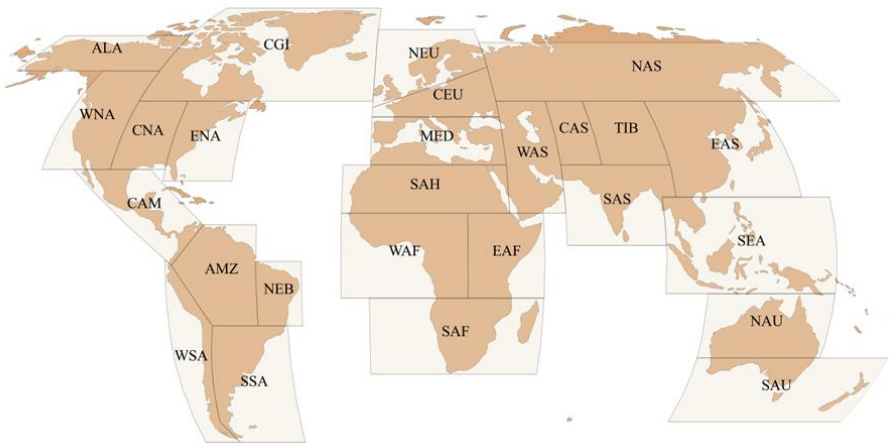


Figure 2. Geographic distribution of 26 regional areas utilized in this study. The regional definitions are adopted from the IPCC Special Report on Managing the Risks of Extreme Events and Disasters to Advance Climate Adaptation (SREX).

3.2. Global Circulation Models (GCMs)

The daily precipitation (Pr), surface air temperature (Tas), and near surface relative humidity ($Hurs$) were obtained from 17 GCMs, each developed by a different modeling institute, using the same initial realization (r1i1p1f1) (see Table 1). We aimed to include as many GCMs as possible; however, at the time of this study, only 17 GCMs provided daily data for all three variables. Additionally, we avoided using multiple GCMs from the same institute to prevent redundancy, as models from the same institute often have similar dynamic and physical parameterizations (Pathak et al., 2023), leading to comparable climate projections (Kuma et al., 2023). All variables obtained from GCMs were interpolated to $1^\circ \times 1^\circ$ resolution using the Inverse Distance Weighting (IDW) method prior to further analysis.

Based on Tas and $Hurs$, the dewpoint temperature ($Tdew$) was developed to serve as

a scaling variable. To be specific, $Tdew$ was calculated by the following formula (Alduchov and Eskridge, 1996):

$$Tdew = \frac{B \times \left(\left(\frac{A \times Tas}{B + Tas} \right) + \log \left(\frac{Hurs}{100} \right) \right)}{A - \left(\left(\frac{A \times Tas}{B + Tas} \right) + \log \left(\frac{Hurs}{100} \right) \right)}$$
 Eq. (1)

where $A = 17.27$ and $B = 237.7$.

Table 1. Summary of the seventeen CMIP6 GCMs utilized study I.

Model	Resolution (lat × lon)	Country
ACCESS-CM2	$1.25^\circ \times 1.875^\circ$	Australia
AWI-CM-1-1-MR	$0.9375^\circ \times 0.9375^\circ$	Germany
CESM2-WACCM	$0.9375^\circ \times 1.25^\circ$	USA
CMCC-ESM2	$0.9375^\circ \times 1.25^\circ$	Italy
CanESM5	$2.8^\circ \times 2.8^\circ$	Canada
EC-Earth3	$0.7^\circ \times 0.7^\circ$	The Netherlands/Ireland
FGOALS-g3	$2.25^\circ \times 2.0^\circ$	China
GFDL-ESM4	$1.0^\circ \times 1.0^\circ$	USA
IITM-ESM	$1.9^\circ \times 1.875^\circ$	India
INM-CM4-8	$1.5^\circ \times 2.0^\circ$	Russia
IPSL-CM6A-LR	$1.25^\circ \times 2.5^\circ$	France
KACE-1-0-G	$1.25^\circ \times 1.875^\circ$	South Korea
MIROC6	$1.4^\circ \times 1.4^\circ$	Japan
MPI-ESM1-2-LR	$1.875^\circ \times 1.875^\circ$	Germany
MRI-ESM2-0	$1.125^\circ \times 1.125^\circ$	Japan
NorESM2-LM	$1.875^\circ \times 2.5^\circ$	Norway
TaiESM1	$0.9375^\circ \times 1.25^\circ$	Taiwan

3.3. Scaling Methods

The scaling rate between daily dewpoint temperature and wet-day precipitation (defined as days with precipitation higher than 0.1 mm/day) was estimated for each grid/region using three different scaling methods: binning with equal bin-width (BW), binning with equal sample data points (BP), and quantile regression (QR). These methods were applied across 31 simulation periods, each spanning 20 years. In other words, we utilized 20 years of continuous data from year $t - 19$ to t (where t ranges from 2060 to 2090) to estimate the scaling rate for each grid/region. In our analysis, the 99th quantile was chosen as the extreme precipitation (PE) index for all three scaling methods. While other high quantiles of precipitation could be selected, we opted for the 99th quantile because it is commonly used in scaling rate estimation (Ali et al., 2018; Wang and Sun, 2022).

For BW, we stratified the precipitation data by dewpoint temperature bins, each with a fixed width of w (defined as 2°C in this study). In each bin, we selected a pair of PE and average dewpoint temperature ($\widehat{T_{dew}}$). Afterwards, the series of $PE - \widehat{T_{dew}}$ pairs obtained from all bins were fitted to a linear regression model, denoted as:

$$\log(PE) = \beta_0 + \beta_1 \widehat{T_{dew}} \quad \text{Eq. (2)}$$

The scaling rate (α_t) of each simulation period from $t - 19$ to t was then obtained by using exponential transformation of the slope coefficient of the model (β_1), as shown in Eq. (3).

$$\alpha_t = 100 \times (\exp(\beta_1) - 1) \quad \text{Eq. (3)}$$

For the second method, BP, the methodology began by categorizing precipitation data based on dewpoint temperature into b equal bins (30 bins used in this study), ensuring each bin contained an equal amount of precipitation data. Subsequently, PE and their corresponding \widehat{Tdew} were selected in each bin. To analyze the relationship between PE and \widehat{Tdew} , we applied locally weighted regression (LOWESS) smoothing (Cleveland, 1979) to the $PE - \widehat{Tdew}$ pairs. LOWESS, recognized for its ability to identify peak-points in scaling with hook-shaped structures, was chosen based on its application in previous studies (Gu et al., 2023; Utsumi et al., 2011). Following the approach outlined by Utsumi et al. (2011), we applied smoothed PE against \widehat{Tdew} before peak-point for the hook-shaped relationships, and across entire series for monotonic relationships. This fitting was performed using a linear model described by Eq. (2), and subsequently, the scaling rate was estimated based on Eq. (3).

Different from the previous two scaling methods, in QR, we fitted the logarithm of PE and \widehat{Tdew} to a linear model based on a conditional quantile. While linear regression considers only the mean of the response variable, QR focuses on a specific quantile of interest (Wasko et al., 2018). The fitting of QR between logarithm of precipitation and dewpoint temperature at q th quantile can be expressed as:

$$\log(PE) = \beta_0^q + \beta_1^q Tdew \quad \text{Eq. (4)}$$

The scaling rate for QR was estimated by the exponential transformation of the slope

coefficient (β_1^q) using Eq. (3).

3.4. Sobol' Sensitivity Analysis

The uncertainty of the scaling rates was decomposed into contributions from different sources using Sobol' sensitivity analysis. Similar to the factorial experimental design of Analysis of Variance (ANOVA), Sobol' sensitivity analysis aims to decompose the variance of model output. However, Sobol' sensitivity analysis is advantageous because it can handle nonlinear relationships (Archer et al., 1997). Moreover, Sobol' sensitivity analysis quantifies the uncertainty contributions from individual sources as well as the higher-order interactions among these sources.

To clarify, if α_t is an ensemble of scaling rate for the period from $t - 19$ to t with total of 153 estimated values, the total variance of α_t can be decomposed to different components, as shown below:

$$V(\alpha_t) = \sum_i V_i + \sum_i \sum_{j>i} V_{ij} + V_{123} \quad \text{Eq. (5)}$$

where $V(\alpha_t)$ is total variance of estimated scaling rates α_t at the t -year-based period. V_i is variance contribution from main sources (future emission scenarios, GCMs and scaling methods), V_{ij} is variance contribution from the interaction between two main sources (future emission scenarios and GCMs, future emission scenario and scaling method, and GCMs and scaling methods), and V_{123} is variance contribution from three main sources.

The sensitivity indices (S) was used to describe how each component contributes to the total variance. It was calculated by dividing both sides of Eq. (5) by $V(\alpha_t)$, as shown:

$$\sum_i S_i + \sum_{i>j} S_{ij} + S_{123} = 1 \quad \text{Eq. (6)}$$

Here, S_i , S_{ij} , S_{123} , are the sensitivity indices for the three individual main sources, interaction between two main sources, and interaction between all three main sources, respectively. If a component with higher sensitivity indices, indicates that it contributes more to the total uncertainty. For a detailed explanation of how $V(\alpha_t)$ is partitioned and how sensitivity indices are computed, refer to Saltelli et al. (2010).

3.5. Framework for Quantifying Numbers of GCMs

GCMs are generally shown to be the primary contributors to the overall uncertainty in the uncertainty decomposition studies (e.g., Ji et al., 2024; Lehner et al., 2020; Wu et al., 2024). Using a small number of GCMs may underestimate the contribution from GCMs (Wang et al., 2020), but using too many GCMs requires more time and may cause computational burden. Hence, it is important to quantify an appropriate amount of GCMs. Here, our objective was to ascertain the optimal number of GCMs for the scaling rate uncertainty decomposition framework, with implications for future reference.

To achieve this goal, we employed the Sobol' sensitivity analysis across all possible combinations of GCMs, exploring subset sizes ranging from 2 to 16 GCMs. This approach allowed us to systematically evaluate how each number of GCMs determine the uncertainty contribution to the overall uncertainty. Instead of arbitrarily selecting samples for each subset, this study calculated the average for every possible combination of GCMs, similar to the approach utilized in Wang et al. (2020) and Zhang et al. (2023). For example, starting with a subset of 2 GCMs, we conducted the Sobol' sensitivity analysis on a total of $C(17,2) = 136$ unique pairs of models. The obtained uncertainty contribution from each number of GCMs were then compared to the contribution from full set of GCMs to identify an optimal number of GCMs. Subsets that exhibited uncertainty contributions comparable to those of the full set of GCMs were considered better subsets in this context.

4. Results

4.1. Uncertainty Decomposition of the Projected Scaling Rates

We start our analysis by presenting the projected average and spread (difference between the 90th and 10th quantiles) across all ensembles for each grid and region over the entire simulation period (2041-2090) to illustrate the spatial distribution of the estimated scaling rates (Figure 3). Several insights emerge from this figure. Firstly, the scaling rates show considerable variability, ranging from -30%/°C to over 10%/°C when analyze on a grid-by-grid-based (see Figure 3a). Negative scaling rates are particularly notable in the intertropical belt at low latitudes, spanning from northern Australia and Southeast Asia to southern India, central Africa, and Brazil in South

America. The lowest scaling rate is observed along the coastal areas of the Brazilian Amazon. Moving towards higher latitudes, higher scaling rates are observed, including ALA and EAS. Moreover, when considering regional scaling rates, the variability tends to decrease, reflecting a more realistic scenario (Figure 3b). Specifically, the scaling rate ranges from -10%/°C to approximately 3%/°C, showing similar spatial patterns as the individual grid scaling rates. In the regional analysis, the CGI region exhibits the highest scaling rate, followed by ALA, EAS, NEU, NAS, and SSA. Conversely, regions located in the intertropical belt such as SEA, EAF, WAF, AMZ, and particularly NEB show the lowest scaling rates. Regional differences in scaling rates can be partly explained by variations in moisture availability. Some regions have sufficient moisture to support increased evaporation and precipitation, while others experience moisture limitations despite rising temperatures. Lastly, a diverse range of grid and regional scaling rates across the ensemble is observed (see Figures 3c and d). In both analyses, areas within the intertropical belt that demonstrates low scaling rates also exhibit considerable variability among the 153 ensembles, likely due to the geographical complexity and the fact that this area is a subsidence zone of Hadley cells, which may affect the performance of GCM simulations. In contrast, higher latitudes generally showed less variability.

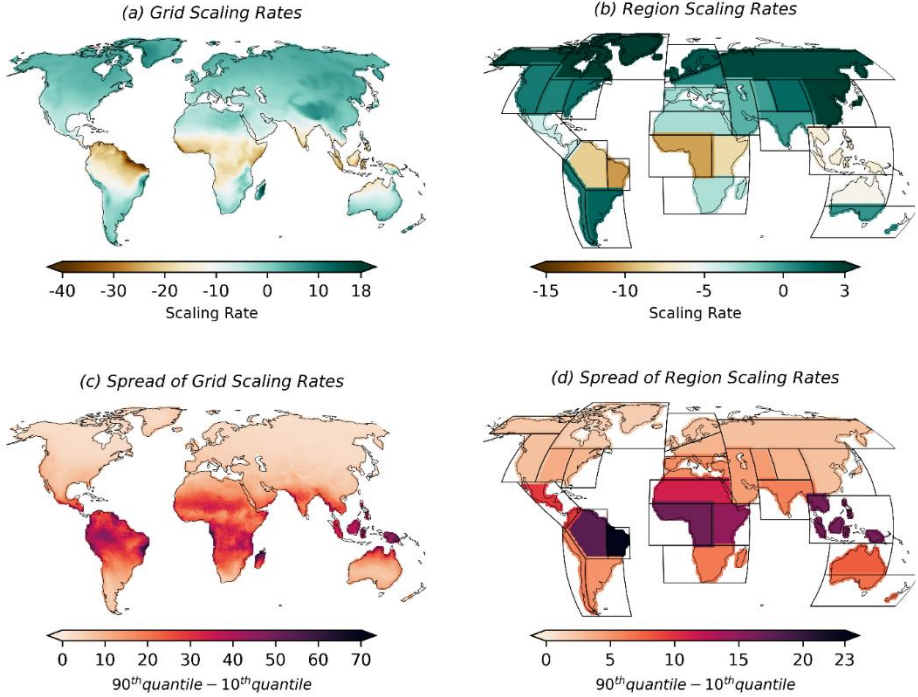


Figure 3. The average of estimated scaling rates and their spread (difference between the 90th and 10th quantile) across 153 ensembles for the entire simulation period (2041-2090): (a) average scaling rates for grids, (b) average scaling rates for regions, (c) spread for grids, and (d) spread for regions.

Given the high spread of the estimated scaling rates, we decompose them into contributions from different sources within the modeling chain. Figure 4 represents the uncertainty contribution from different sources for each grid throughout the entire simulation period. Specifically, Figures 4a-c illustrate the uncertainty contribution from three main sources, while Figures 4e-f show the interactions between two main sources. The values displayed in the box at the bottom left of each panel represent the global averages. GCMs are the primary contributor to the overall uncertainty across most regions worldwide, with the highest contribution observed in areas with geographical complexity such as the Tibetan Plateau of China. This leads to a high

global average contribution of 40.38% to the overall uncertainty from GCMs. The scaling method plays the second most significant role, contributing an average of 13.71% globally to the overall uncertainty. High contributions from both sources also result in a somewhat elevated contribution from the interaction between GCMs and scaling methods, averaging 17.37% globally. In contrast, future emission scenarios contribute minimally, with a global average of only 2.70%, suggesting that the choice of future emission scenarios may have relatively less impact on future projections.

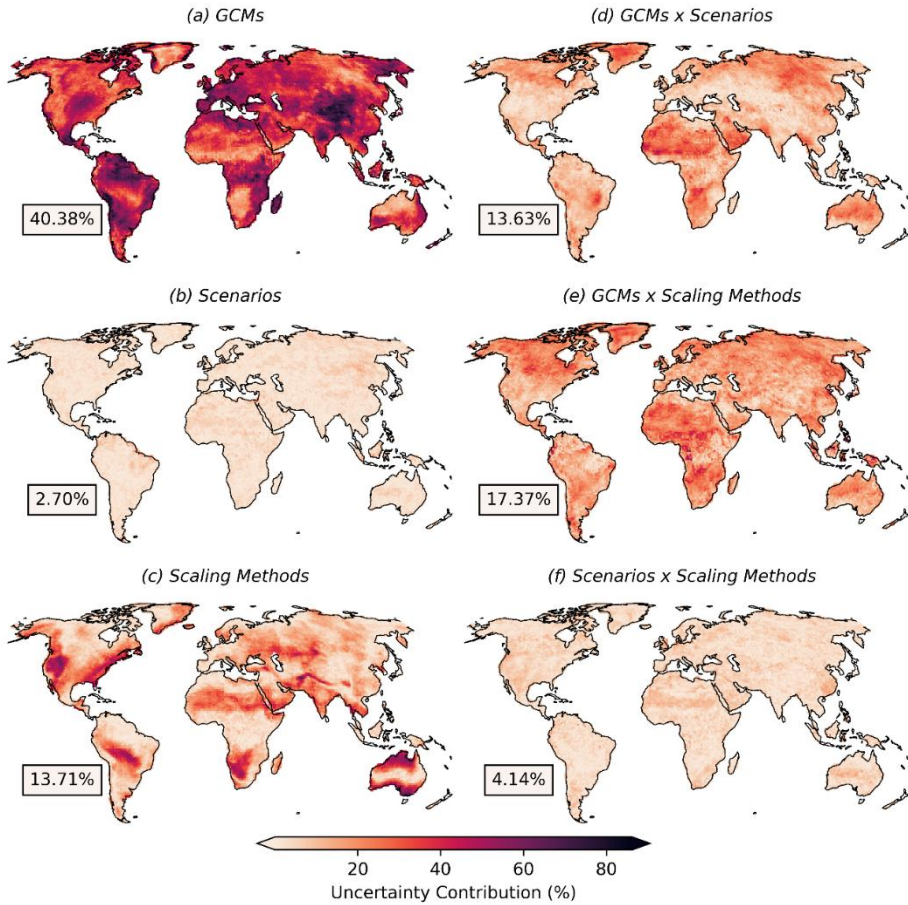


Figure 4. Global uncertainty contributions from each source: (a) GCMs, (b) future emission scenarios, (c) scaling methods, (d) interaction between GCMs and future emission scenarios, (e) interaction between GCMs and scaling methods, and (f) interaction between future emission scenarios and scaling methods. The values in the box at the bottom left of each panel represent the global average across all grid points.

Subsequently, we examine the uncertainty contribution from each source to the overall uncertainty across all regions and simulation periods. Figure 5 displays 6 out of 26 regions along with the global average, while the remaining 20 regions are illustrated in Figure 6. Generally, GCMs are the predominant source of uncertainty throughout all simulation periods, except for AMZ, NAS, NEB, SAU, and WAF, where scaling

methods have a greater contribution. EAS shows the highest contribution from GCMs and the lowest from scaling methods, averaging 68.32% from GCMs and 0.85% from scaling methods over the simulation periods. Conversely, WAF exhibits the lowest contribution from GCMs at 27.59%, whereas SAU has the highest contribution from scaling methods, averaging 51.13%. Future emission scenarios contribute minimally to the uncertainty from scaling rates across all regions but have a more notable effect when interacting with GCMs. The interaction between the GCMs and scaling methods also contributes significantly in some regions. Specifically, in regions like MED, SAS, and CEU, it contributes almost 30%. This suggests that when estimating scaling rates, it is important to consider multiple scaling methods, as their interaction with GCMs is non-linear, and relying on just one method could lead to misinterpretation of the results. Upon reviewing the temporal changes in uncertainty contributions, we found that the contribution from all sources remained relatively stable across all 31 simulation periods for all regions, with only minor variations. Notably, the contribution from future emission scenarios increases in the far future for certain regions, such as NAU, CEU, CNA, TIB, and SAU. The contribution from scaling methods remains consistent through most simulation periods, though they decrease over time in regions like WAF, WSA, and CEU, while showing an increasing trend in regions such as SAF, NAU, SSA, and SAH. GCMs also exhibit minimal variation, generally decreasing in regions like WNA, SEA, SAH, and CEU. However, it is worth noting that the changes in contribution from all sources are minor, leading to a stable global average, as depicted in Figure 5g. On a global scale, GCMs consistently account for the highest uncertainty contribution at 46.82%, followed by scaling methods at 23.75%, and the interaction between GCMs and scaling methods at 19.83%. Future emission scenarios, along with

their interactions with GCMs and scaling methods, contribute modestly to the overall uncertainty.

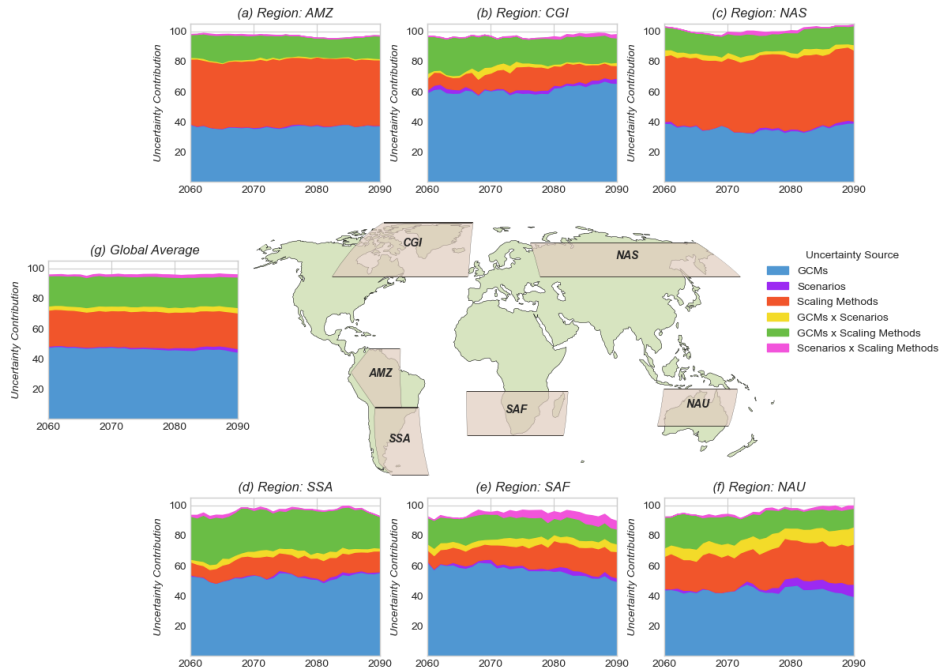


Figure 5. Uncertainty contribution from all sources for six regions: (a) AMZ, (b) CGI, (c) NAS, (d) SSA, (e) SAF, and (f) NAU; along with (g) the global average. In each panel, colors represent the uncertainty contribution from different sources: blue for GCMs, purple for future emission scenarios, red for scaling methods, yellow for interactions between GCMs and future emission scenarios, green for interactions between GCMs and scaling methods, and pink for interactions between future emission scenarios and scaling methods.

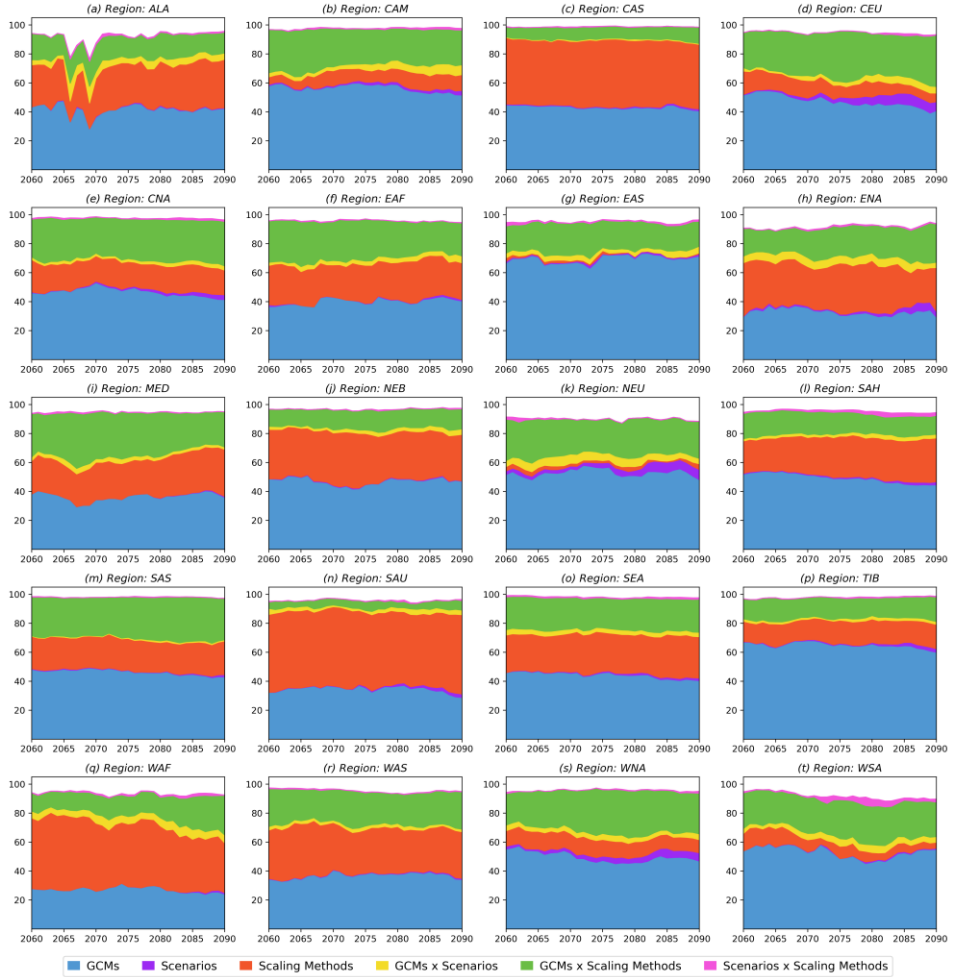


Figure 6. Same as Figure 5, but for the remaining 20 regions.

4.2. GCM Quantity in the Uncertainty Decomposition Framework

GCMs are the major source of the uncertainty of estimated scaling rates in most regions, as noted in the previous section. Here, we explore the optimal number of GCMs required to achieve robust results within this uncertainty decomposition framework. Figure 7 displays the uncertainty contribution from GCMs, averaging all possible

combinations of GCMs (ranging from 2 to 17) across all simulation periods for 6 regions and globally for all the simulation periods. The other 20 regions are shown in Figure 8. From Figures 7a and 8, it is observed that with a low number of GCMs, the framework underestimates the uncertainty contribution from GCMs. However, as the number of GCMs increases, their contribution to the uncertainty also increases across all regions. Generally, when the number of GCMs is increased to 8 or 9, their contribution to the uncertainty starts to approach the $\pm 5\%$ range of uncertainty contribution from 17 GCMs. To be specific, the framework requires at least 8 or 9 GCMs to be robust for 22 out of 26 regions. However, for the remaining four regions, additional GCMs are required: the framework needs at least 11 GCMs for NAS, 10 for SAF, and 14 each for both ALA and WSA. For the global average, similar interpretation can be found. In all simulation periods, the contribution from GCMs increases with the number of GCMs utilized. Using only 2, 3, or 4 GCMs results in a notably low contribution. When 9 GCMs are used, the uncertainty contribution from GCMs falls in the $\pm 5\%$ range of the 17 GCMs for all the simulation periods. For GCM counts from 9 to 16, the uncertainty contribution consistently falls within this range. Specifically, the average difference in uncertainty contribution between using 17 GCMs and 2 GCMs is 20.61%, while the difference between using 17 GCMs and 9 GCMs is only about 1.71%.

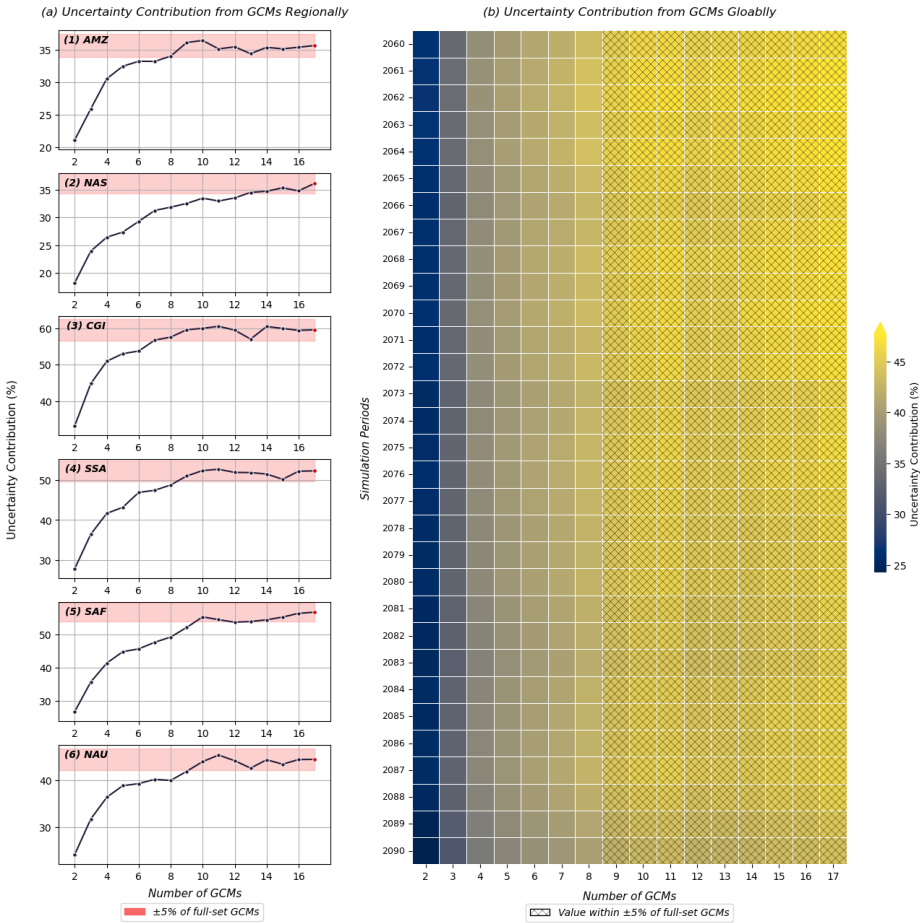


Figure 7. Uncertainty contribution from varying numbers of GCMs, ranging from 2 to 17. (a) Average uncertainty contribution over 31 simulation periods from GCMs of 6 regions that were presented in Figure 4. Each scatter point represents the average values of all possible combination pairs taken from the 17 GCMs. The shaded red line denotes the $\pm 5\%$ of uncertainty contribution from the 17 GCMs, represented by red points. (b) Globally averaged uncertainty for each simulation period. The hatch in each cell of the heat map indicates values within $\pm 5\%$ of uncertainty contribution from the 17 GCMs.

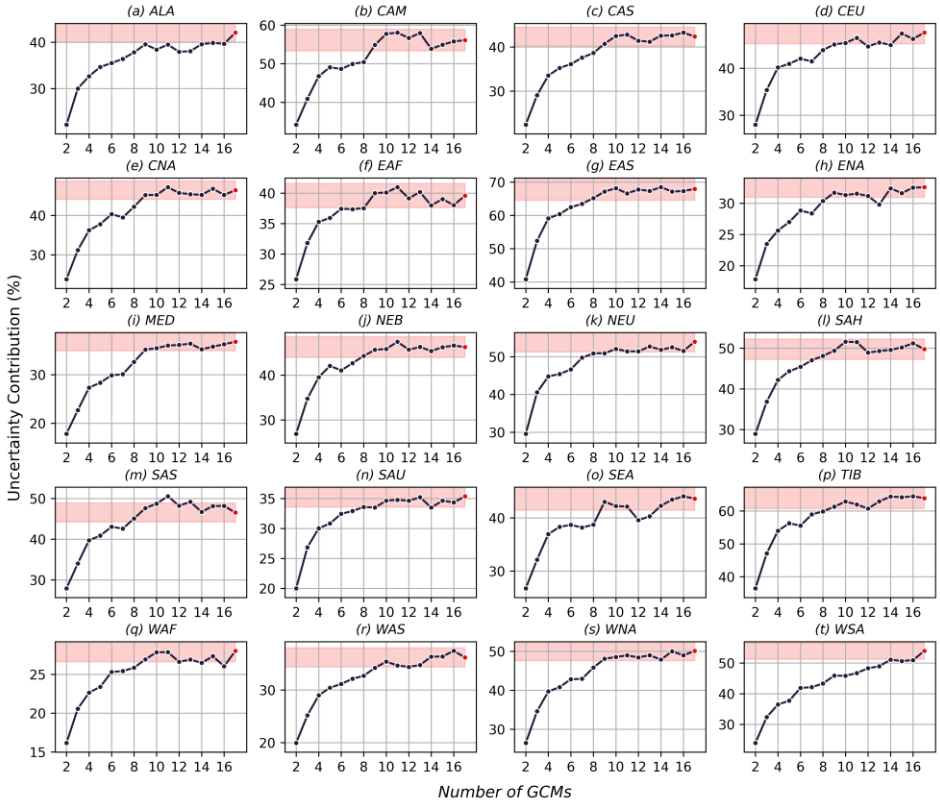


Figure 8. Same as Figure 7a, but for the remaining 20 regions.

Next, we investigate the impact of the number of GCMs on other sources of uncertainty by selecting sample combinations for each possible number of GCMs used. The sample selection approach is as follows: First, we group all combinations of each number of GCMs based on the individual GCMs contained within those combinations. Each group corresponds to combinations that share a common GCM. Then, from each group, we randomly select one combination. This process ensures that for each number of GCMs, we obtain 17 samples (one from each group corresponding to each GCM). For example, when the number of GCMs is 2, the first group will contain combinations

such as (ACCESS-CM2, AWI-CM-1-1-MR), (ACCESS-CM2, CESM2-WACCM), and so on. Within this group, we randomly select one sample. We repeat this process for all the other 16 groups. This approach allows us to explore the uncertainty contribution more comprehensively across different numbers of GCMs, by capturing a representative subset of combinations without biasing the results toward certain combinations. Figure 9 illustrates the distribution of sampled combinations for seven different GCM sample sizes (2, 5, 9, 10, 12, 14, 16) across six regions, as shown in Figures 5 and 6. The remaining 20 regions are presented in Figure 10. The results indicate that for all regions, a low number of GCMs (e.g., 2, 5) leads to significant disagreement among the combinations. For example, in the NAU region, using only 2 GCMs results in high variability, with some combinations indicating that GCMs are the largest source of uncertainty, while others suggest that scaling methods dominate. This variability highlights that with fewer GCMs, the contribution of GCMs to overall uncertainty is underestimated, leading to an overestimation of the uncertainty attributed to scaling methods. Additionally, the contribution from future emission scenarios and their interaction with scaling methods is also exaggerated under low GCM conditions. However, as the number of GCMs increases, the agreement among combinations improves, especially from 9 GCMs onward, where most regions exhibit consistent uncertainty distribution patterns. Therefore, when decomposing the uncertainty of scaling rates for extreme precipitation using CMIP6 data, researchers should consider using a sufficient number of climate models, with at least 9 GCMs recommended.

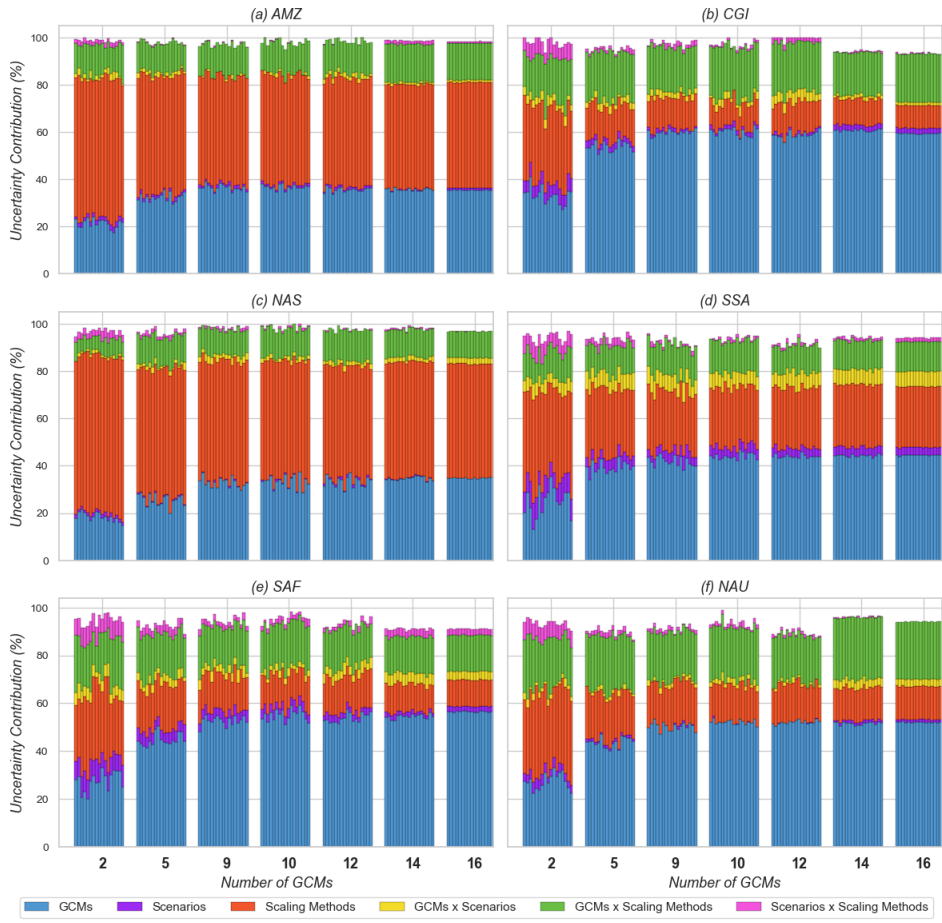


Figure 9. Distribution of uncertainty contributions across six regions: (a) AMZ, (b) CGI, (c) NAS, (d) SSA, (e) SAF, and (f) NAU for different numbers of GCMs (2, 5, 9, 10, 12, 14, 16): Each bar represents a sample from combinations within each group of each number of GCM.

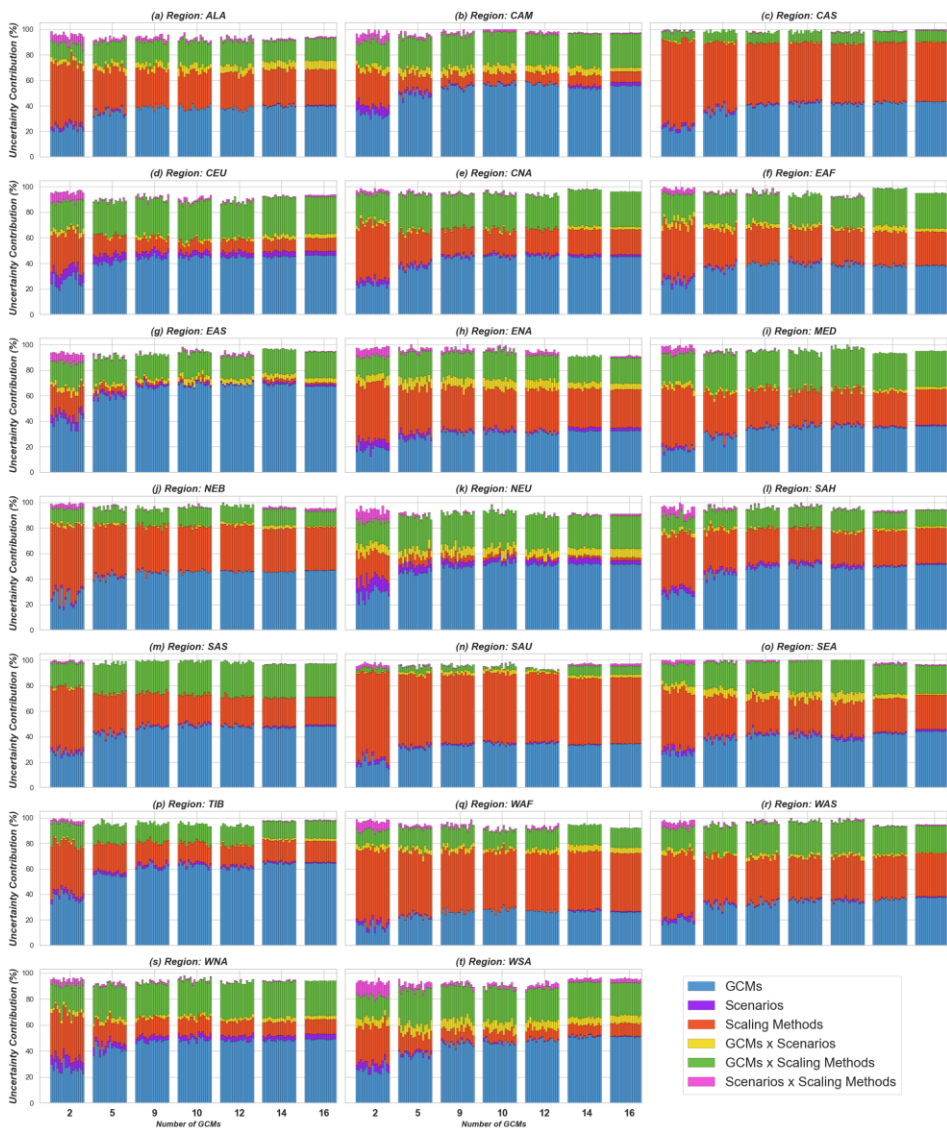


Figure 10. Same as Figure 9, but for the remaining 20 regions.

4.3. A Comparison Between CMIP5 and CMIP6

In this section, we analyze data from CMIP5 and compare it with CMIP6 to evaluate the differences in the contribution of each uncertainty source to overall uncertainty. Based on the findings from the previous section, where it was determined that at least 9 GCMs are necessary for a robust uncertainty decomposition, we use 10 GCMs from CMIP5. These GCMs are analyzed across three future emission scenarios—RCP26, RCP45, and RCP85—representing low, medium, and high greenhouse gas emissions, respectively. Detailed information on the selected 10 GCMs is provided in Table 2.

Table 2. Summary of the ten CMIP5 GCMs utilized in study I.

Model	Resolution (lat × lon)	Country
BU-ESM	$2.8^\circ \times 2.8^\circ$	China
CNRM-CM5	$1.4^\circ \times 1.4^\circ$	France
CSIRO-Mk3-6-0	$1.9^\circ \times 1.9^\circ$	Australia
CanESM2	$2.8125^\circ \times 2.8125^\circ$	Canada
GFDL-ESM2G	$2.0^\circ \times 2.5^\circ$	USA
HadGEM2-ES	$1.25^\circ \times 1.875^\circ$	UK
IPSL-CM5A-LR	$1.9^\circ \times 3.75^\circ$	France
MIROC5	$1.4^\circ \times 1.4^\circ$	Japan
MRI-CGCM3	$1.125^\circ \times 1.125^\circ$	Japan
NorESM1-M	$2.0^\circ \times 2.0^\circ$	Norway

In Figure 11, we recreate Figure 3 to compare the differences between estimated scaling rates globally and regionally, both in terms of the average and the spread among the 90 ensembles. The results indicate that the average scaling rates and their spread exhibit a similar spatial distribution globally similar to those in CMIP6. Negative scaling rates are observed in the intertropical belt, with the lowest values along the coastal areas of the Brazilian Amazon, while higher scaling rates are prevalent in higher latitude regions. However, it is important to note that in CMIP5, the maximum spread is greater than in CMIP6, highlighting significant variability between the ensembles. Regionally, the estimated scaling rates show similar spatial patterns, with the lowest values in WAF and the highest spread consistent with CMIP6 observed in NEB and SEA.

To understand the spatial distribution of uncertainty contributions from all sources in CMIP5, we decompose the uncertainty in scaling rates across the 90 ensembles and recreate Figure 4, as illustrated in Figure 12. The results show that the spatial distribution of uncertainty contributions in CMIP5 is similar to that in CMIP6. Specifically, GCMs contribute to the overall uncertainty the most at 44.95%, while scaling methods and their interaction with GCMs contribute 17.26% and 15.11%, respectively. Future emission scenarios contribute a relatively low 3.04%, which is higher than their interaction with scaling methods (2.83%) but lower than their interaction with GCMs (11.36%). Figure 13 compares the uncertainty contributions from each source between CMIP6 and CMIP5, showing the differences (CMIP6 – CMIP5). The results indicate that the largest difference is in the contributions from GCMs, with CMIP5 GCMs contributing 4.57% more globally than those in CMIP6.

Spatially, CMIP5 shows higher contributions in regions such as central to northern Australia, northeast China to southeast Russia, southern and central Africa, and Canada. Conversely, GCMs from CMIP6 contribute more in regions like Brazil, India, the Middle East, and Europe. Future emission scenarios show the smallest difference between the two CMIP phases, with a global average difference of 0.75%, where CMIP5 has a slightly higher contribution. For scaling methods, CMIP5 exhibits a global average difference of 3.72%, indicating a higher contribution compared to CMIP6. This increased contribution is particularly evident in regions such as the southern Middle East, northern Africa, Greenland, Alaska, and the northeastern USA and Europe. Notably, all three main sources contribute more globally in CMIP5 than in CMIP6. However, interactions between these sources contribute more in CMIP6 compared to CMIP5. Specifically, interactions between GCMs and future emission scenarios, GCMs and scaling methods, and future emission scenarios and scaling methods in CMIP6 show greater contributions in most parts of the world, with global averages of 2.29% and 2.24%, respectively.

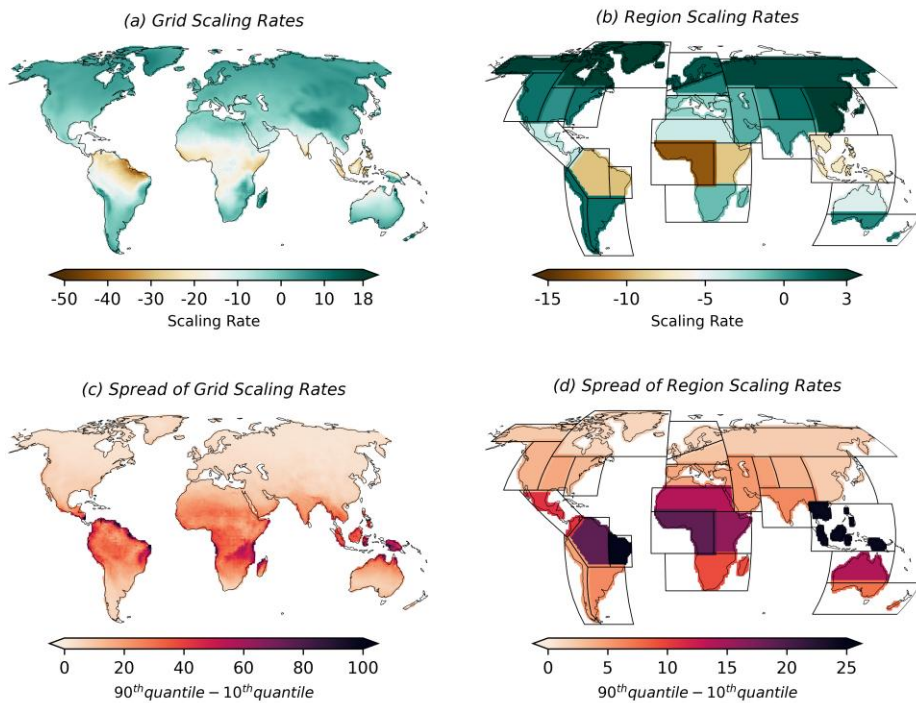


Figure 11. Same as Figure 3, but for CMIP5.

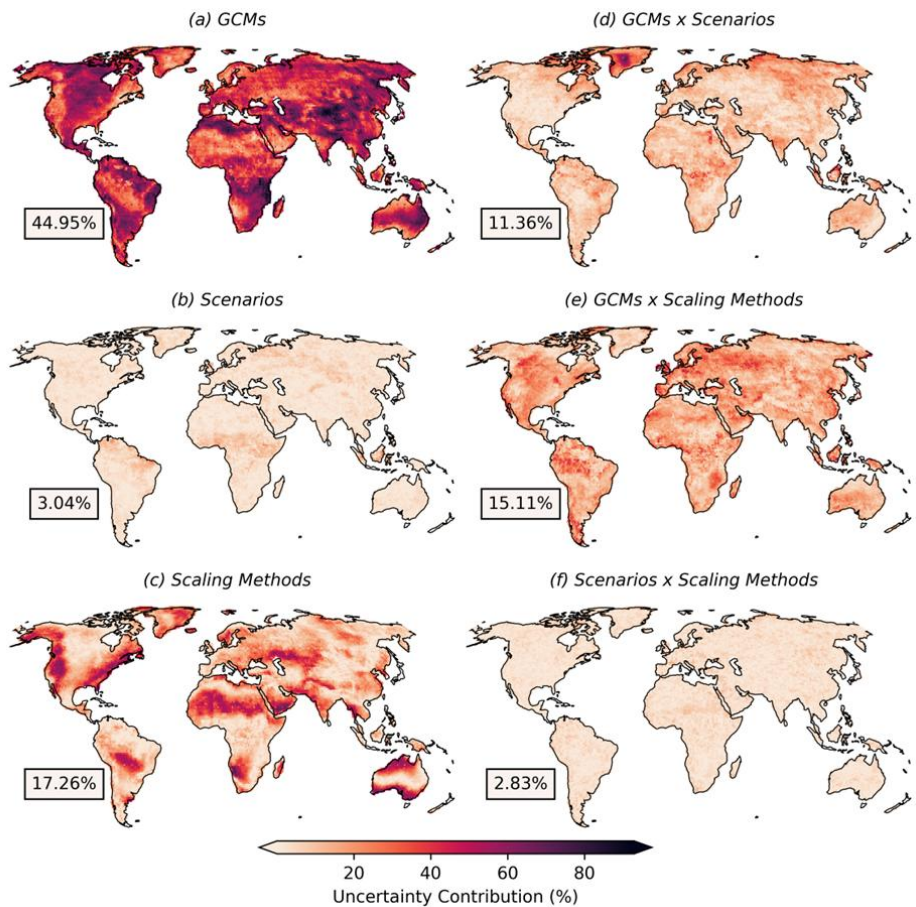


Figure 12. Same as Figure 4, but for CMIP5.

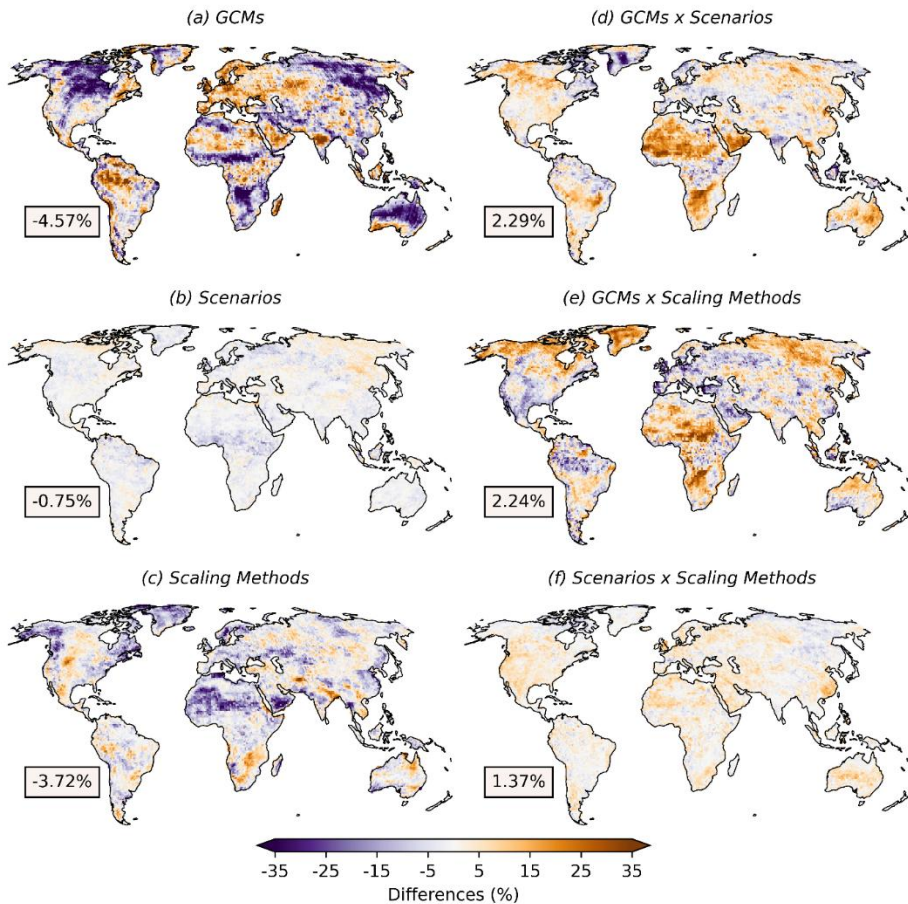


Figure 13. The differences of the uncertainty contribution of each source between CMIP6 and CMIP5 (CMIP6-CMIP5). (a) GCMs, (b) future emission scenarios, (c) scaling methods, (d) interaction between GCMs and future emission scenarios, (e) interaction between GCMs and scaling methods, and (f) interaction between future emission scenarios and scaling methods. Purple color indicates negative values, where an uncertainty source contributes in CMIP5 more than in CMIP6, while orange indicates the opposite. The values in the box at the bottom left of each panel represent the global average across all grid points.

Figure 14 presents the uncertainty decomposition of estimated scaling rates across each simulation period for all regions using CMIP5 data. The results indicate that GCMs are the highest contributors in most regions, except for AMZ, ENA, NAS, and SAU, where scaling methods contribute more, and NEU and WSA, where the interaction between GCMs and scaling methods has a higher contribution. Future emission scenarios contribute very little to overall uncertainty in all regions. Temporal changes are also found here, particularly for future emission scenarios, which show an increase over time in regions such as CEU, CGI, EAS, ENA, NAS, NEU, TIB, and WNA. For GCMs, the temporal changes vary by region. In CAM, SSA, and WNA, the contribution from GCMs decreases slightly around 2080 but increases again after 2085. Conversely, the contributions from GCMs tend to decrease in regions like ALA, CGI, EAS, WNA, NAS, and WAF, while increasing in CEU, MED, SAF, and SAU. It should be highlighted that in CMIP5, the interaction between main sources contribute more than in CMIP6, notably the interaction between GCMs and future emission scenarios as well as GCMs and scaling methods.

The differences in uncertainty contributions from each source between CMIP6 and CMIP5 are presented in Figure 15. The first column displays regional differences, and the second column shows the globally averaged differences for each simulation period. For the regional differences, it is observed that the differences between CMIP6 and CMIP5 are significant for GCMs and scaling methods. The average difference for GCMs reaches as high as 30% in NAS and drops to -20% in WNA and TIB. For scaling methods, the differences exceed -20% in AMZ, ENA, and NAS and reach 20% in EAS and NEU. The interactions between GCMs with scaling methods and future emission

scenarios also show considerable differences between the two phases of CMIP. For example, in CGI, the difference exceeds -20% for the interaction between GCMs and future emission scenarios, while in WSA, it reaches -20% for the interaction between GCMs and scaling methods. Future emission scenarios and their interaction with scaling methods exhibit minimal differences between CMIP6 and CMIP5, with the highest difference for future emission scenarios being -10% in CGI, and the interaction with scaling methods shows differences around 1% to -1%. To be specific, CMIP6 has higher contributions to the overall uncertainty than CMIP5 in 12 out of 26 regions for GCMs, 19 regions for future emission scenarios, 16 regions for scaling methods, 9 regions for the interaction between GCMs and future emission scenarios, 8 regions for the interaction between GCMs and scaling methods, and 23 regions for the interaction between future emission scenarios and scaling methods. From the global averaged perspective in each simulation period, the differences are not significant in all simulation periods for the GCMs. However, the spread is huge, ranging from -20% to 20%. While for future emission scenarios, the difference is found, but not a huge percentage. The differences in future emission scenarios in CMIP6 contribute more than in CMIP5 before 2076 but turn lower than in CMIP5 after 2080, while for the differences in the scaling methods, it is found that in CMIP6 is higher than in CMIP5 in all simulation periods. For the interactions between main sources, interaction between GCMs and future emission scenarios contribute less in CMIP6 than in CMIP5 in all simulation periods, while future emission scenarios and scaling methods contribute more in CMIP6 than in CMIP5. Interaction between GCMs and scaling methods shows no significant differences.

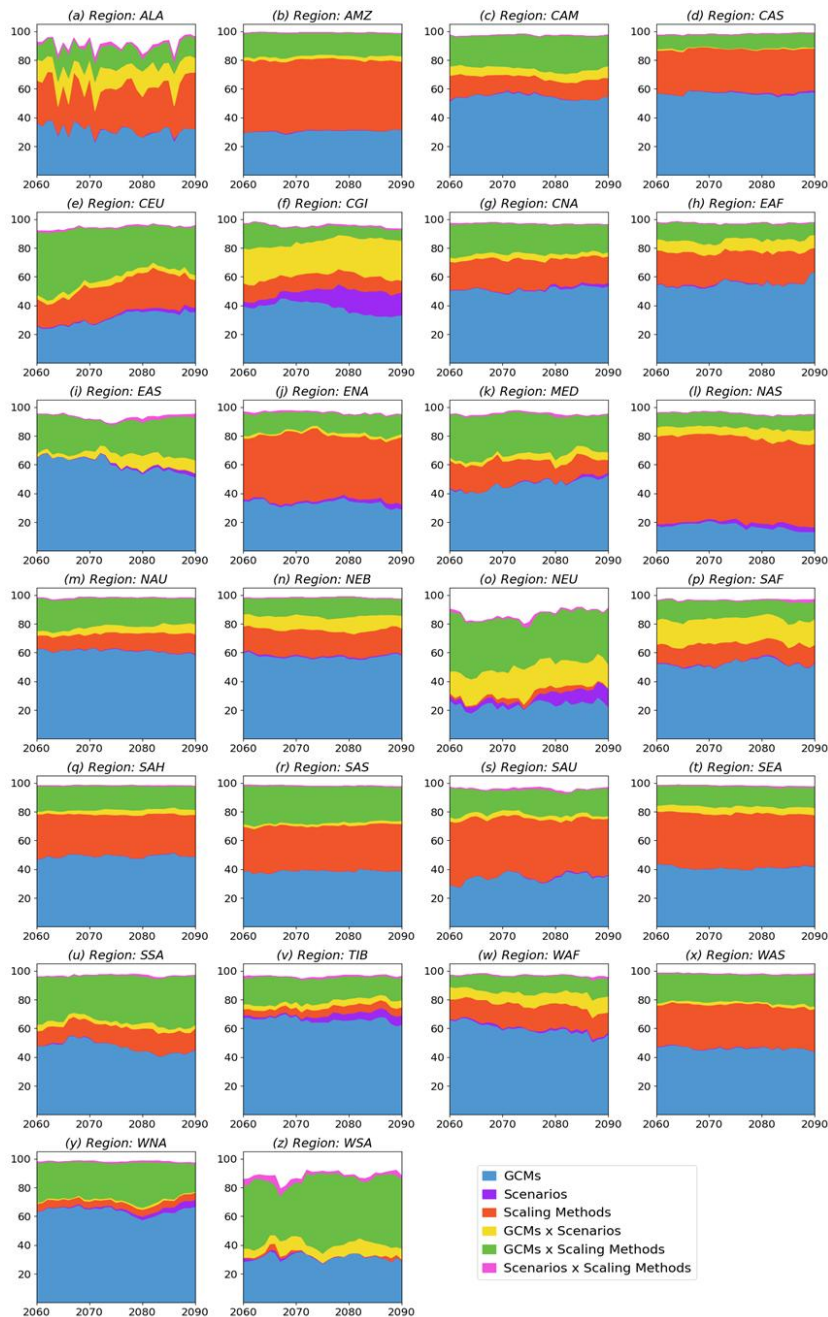


Figure 14. Same as Figure 6, but for 26 regions of CMIP5.

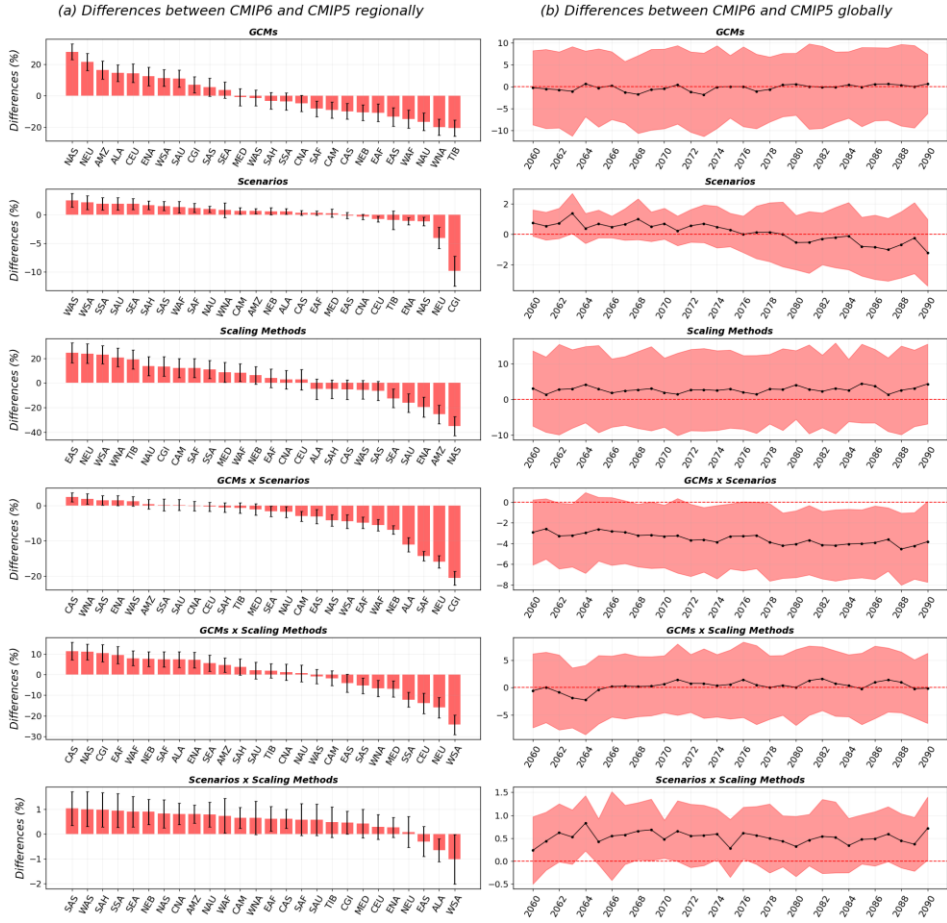


Figure 15. Differences in uncertainty contributions between CMIP6 and CMIP5 (CMIP6 - CMIP5). The first column illustrates regional differences, with bars indicating the average across all simulation periods and error bars representing the magnitude of the standard deviation. The second column depicts global averages for each simulation period, with a line plot showing the average value and a shaded red area indicating the magnitude of the standard deviation.

5. Discussions

Many studies about uncertainty decomposition for future climate projections have been conducted for different climate variables. This study contributes to this field by decomposing the uncertainty of scaling rates of extreme precipitation. Despite focusing on different climate variables, our findings are largely consistent with previous studies, showing only slight deviations. For instance, similar to past studies (Lehner et al., 2020; Wu et al., 2024; Zhang et al., 2023; Ji et al., 2024), our analyses show that GCMs are the biggest contributor to the overall uncertainty. However, future emission scenarios, which play a significant role in other studies (Lehner et al., 2020; Zhang and Chen, 2021), contribute minimally to scaling rates uncertainty. This may be because the changing rates of extreme precipitation do not depend heavily on the forcing scenarios, as extreme precipitation is primarily driven by the amount of moisture in the atmosphere which is related to total warming of climate models rather than the specific greenhouse gases or other forcing components (Li et al., 2021; Pendergrass et al., 2015; Seneviratne et al., 2016). On the other hand, scaling methods also play a substantial role in some regions, sometimes surpassing GCM contributions, highlighting their importance in scaling rate estimations, consistent with the findings of Ali et al. (2022) and Fowler et al. (2021). Moreover, this study indicates that an insufficient number of GCMs may pose challenges in achieving robust in overall uncertainty decomposition. The analysis on quantifying the number of GCMs needed in the uncertainty decomposition framework suggests a recommendation that is only one GCM lower than that of Wang et al. (2020), who recommended using 10 GCMs for hydrological impact studies. Despite differences in frameworks and variables of interest, their results align closely with ours, reinforcing our recommendation. Although we suggest

9 GCMs as the optimal number for achieving robust results across the majority of regions and global averages for each simulation period, we recognize that certain regions exhibit notable variations. Specifically, ALA and WSA require 14 GCMs, NAS needs 13 GCMs, and SAF requires 10 GCMs.

In addition to our primary findings with CMIP6, we compare these results to those of CMIP5 at grid, regional, and temporal scales. In line with previous studies (Wu et al., 2024; Zhang and Chen, 2021), the grid-based analysis shows that CMIP5 and CMIP6 exhibit similar spatial patterns, with GCMs being the largest contributors to the uncertainty. However, regional differences in GCM contributions between CMIP5 and CMIP6 varies, with discrepancies exceeding 20% in some regions. Notably, the average differences on a grid-based indicate that GCMs in CMIP5 contribute more than those in CMIP6, as well as in 15 out of 26 regions, suggesting that GCMs in CMIP6 have a narrower spread compared to CMIP5. This is a positive sign of improvement of the generation of CMIP, as a lower spread suggests lower uncertainty in the projected climate variables. Several studies have also demonstrated the lower spread of CMIP6 GCMs across various climate variables (Chen et al., 2021; Martel et al., 2022; Li et al., 2020). For regions and grids where GCMs in CMIP6 contribute more than those in CMIP5, this is likely due to the inclusion of more complex physical parameterizations in CMIP6 (Eyring et al., 2016), which may increase the model disagreement. Interestingly, the global average reveals little change in GCM contributions, but CMIP6 shows lower contributions from future emission scenarios in the far future, though the difference is negligible (about 1-2%). This aligns with Miao et al., 2023, who observed that by the end of the century, future emission scenarios in

CMIP5 contributed more to runoff uncertainty than those in CMIP6.

6. Conclusions of Study I

This section, we aimed to understand the uncertainty in estimated scaling rates arising from three main sources: GCMs, future emission scenarios, and scaling methods, as well as their interactions within each source. The analysis began by estimating scaling rates for all 31 simulation periods from each GCM under all future emission scenarios and scaling methods for grids across the global land area. These grids were then aggregated to determine regional scaling for 26 regions. Using data projected from 2040 to 2090 across 17 GCMs, three future emission scenarios, and three scaling methods, we analyzed 153 ensemble members for each grid and region. The uncertainty in the ensembles was decomposed into contributions from the three main sources and their interactions. Furthermore, the study evaluated the optimal number of GCMs needed for robust uncertainty decomposition by analyzing all possible GCM combinations. A comparison with CMIP5 was also conducted to better understand the differences between the two CMIP generations.

The findings of this study can be summarized as follows. First, the projected global scaling rates show a median with a slight decreasing trend over time, while regional scaling rates vary widely, encompassing both positive and negative values. Second, the uncertainty decomposition of scaling rates indicated that GCMs were the primary contributors to uncertainty across most regions, both at the grid and regional levels. While scaling methods and their interactions with GCMs also had a significant impact,

future emission scenarios contributed minimally. Third, incorporating a large number of GCMs in the analysis can enhance its robustness, but it may also add to the computational load. Conversely, using too few GCMs can compromise the robustness of the results. The study systematically showed that incorporating fewer GCMs in the uncertainty decomposition framework led to an underestimation of GCM contributions and an overestimation of the effects of scaling methods and future emission scenarios. To ensure robust analysis, the study recommends including at least nine GCMs in future scaling projections. Lastly, comparisons between CMIP5 and CMIP6 revealed slight differences in uncertainty contributions from each source. For grid scaling, CMIP5 exhibited higher uncertainty contributions from main sources compared to CMIP6, which had more significant interaction effects. In regional scaling, while differences varied by region, no substantial global differences were observed.

IV. Study II: Uncertainty Decomposition of Changes in Extreme Precipitation

1. Introduction

Extreme precipitation was understood to have two main components that influenced its intensity: dynamic processes (*DY*) and thermodynamic processes (*TH*) (Trenberth et al., 2003). *TH* mainly refers to the relationship between atmospheric warming and moisture content, as described by the Clausius-Clapeyron (CC) relation. As global temperatures are projected to rise in the future, the atmosphere is expected to hold more moisture, thereby intensifying extreme precipitation events (Li et al., 2025). On the other hand, *DY* are associated with vertical air motion, which is influenced by local and large-scale atmospheric circulation patterns (O’Gorman and Schneider, 2009). Under climate change conditions, both *TH* and *DY* processes are expected to change, making future changes in extreme precipitation particularly difficult to project (Paik et al., 2023).

With an effort to study both component of extreme precipitation, Emori and Brown (2005) suggested a statistical model to separate these two components in order to better understand their mechanisms. The study used empirical correlations between precipitation amount and vertical wind velocity at 500 hPa to separate the components. However, it was found that this method was not applicable in some regions, where the correlation between precipitation and vertical wind velocity was weak, such as in the subtropics (Pfahl et al., 2017). To address this limitation, O’Gorman and Schneider

(2009) introduced the physical scaling diagnostic, which separated the components by mass-weighted integration of vapor content through vertical pressure levels. This approach has been widely used in studies aimed at understanding the processes of extreme precipitation (e.g., Dai et al., 2024; Huang et al., 2023; Li et al., 2025; Ritzhaupt and Maraun, 2024).

Changes in extreme precipitation are often assessed by comparing historical and future simulations of extreme indices such as $Rx1Day$, typically expressed as either relative or absolute differences. Past studies have found significant increases in $Rx1Day$, particularly along the Intertropical Convergence Zone, central Africa, the polar regions, and parts of the Pacific, alongside notable decreases over oceanic regions such as the central Atlantic and the Pacific near South America (Dai et al., 2024; Dai and Nie, 2021; Li et al., 2025; Paik et al., 2023). However, these studies also revealed that regions exhibiting pronounced increases or decreases in $Rx1Day$ were associated with high uncertainty and substantial disagreement among simulations. When decomposing these changes into DY and TH components, it was found that TH generally led to increases in $Rx1Day$ across all regions at a relatively consistent rate as expected from CC relation. In contrast, DY is primarily responsible for the pronounced regional differences, including both increases and decreases. Regarding uncertainty, the thermodynamic contribution is more evident in the mid- to high latitudes, whereas the dynamic component exhibits high uncertainty across the globe (Dai and Nie, 2021; Li et al., 2025).

2. Objectives

Although several studies have investigated the uncertainty in both thermodynamic (*TH*) and dynamic (*DY*) components of extreme precipitation and found that both contribute to uncertainty in changes of *Rx1Day*, none have decomposed the sources of uncertainty within each component individually. As highlighted by Hawkins and Sutton (2009), the three major sources of uncertainty in climate projections are climate models, emission scenarios, and internal variability. Understanding how each of these sources contributes to the uncertainty in *TH* and *DY* components is crucial for guiding future research, informing policymakers, and supporting climate model development. In addition, Hawkins and Sutton (2009) introduced the *SNR* as a useful metric for evaluating the robustness of projected changes—indicating the extent to which the underlying signal can be distinguished from the uncertainty (noise). By evaluating the *SNR* over the projection period, it is also possible to identify when uncertainty dominates the signal and when the signal becomes sufficiently clear to inform decision-making and policy development (Zhang and Chen, 2021). However, to the best of my knowledge, previous studies have not yet investigated the *SNR* of *TH* and *DY*, nor how the noise in *TH* and *DY* affects the signal of the overall changes.

To tackle the gaps left by past literature, this section seeks to answer the following research questions:

1. What are the projected global changes in *Rx1Day*, and how do the *TH* and *DY* components contribute to these changes?

2. How do the three uncertainty sources contribute to the total uncertainty in $Rx1Day$, TH , and DY ?
3. What is the SNR in TH , and DY , and how does uncertainty (noise) in each component influence the detectability of the true change signal?

3. Data and Methods

In this section, we utilize simulations from 20 General Circulation Models (GCMs) participating in CMIP6, each under three future emission scenarios. Since the HS09 framework is applied for uncertainty decomposition, only one ensemble member per model is required. The analysis covers two time periods: a historical baseline from 1971 to 2000, and a future projection period from 2021 to 2100. We first decompose the projected changes in $Rx1Day$ into TH and dynamic DY components using the physical diagnostic method. Subsequently, we apply the HS09 approach to quantify the contributions of different uncertainty sources to changes in $Rx1Day$, TH , and DY .

We consider the whole global area for investigation, including polar regions and oceans. Oceans are included because previous studies have shown that the most pronounced increases and decreases in $Rx1Day$ often occur over the oceans (Dai et al., 2024; Dai and Nie, 2021; Li et al., 2025; Paik et al., 2023). Furthermore, this analysis incorporates internal variability into the uncertainty decomposition, as temperature and precipitation variability are often more pronounced over oceanic regions (Zhang and Chen, 2021). Therefore, including the oceans is

essential for a comprehensive understanding of these changes.

3.1. Future Emission Scenarios and GCMs

In this section, we use the same three emission scenarios as in the previous analysis: SSP1-2.6, SSP2-4.5, and SSP5-8.5. These scenarios are selected as they represent a broad range of possible future socioeconomic and emission pathways, from low to high greenhouse gas concentrations. For detailed descriptions of each scenario, please refer to the previous section.

The selection of GCMs in this section differs slightly from the previous analysis. While the previous section included only one model per modeling center, this section includes all available models that provide the necessary variables—such as vertical wind velocity and temperature at pressure levels—which are required for the physical decomposition of extreme precipitation. Due to the limited availability of these variables, especially across the required time periods (1971–2000 for historical and 2021–2100 for projections) and scenarios (SSP1-2.6, SSP2-4.5, and SSP5-8.5), model selection was based solely on data availability. In total, 20 GCMs met these criteria and were included in the analysis. For each model, four daily variables were obtained: vertical wind velocity (*wap*), temperature at pressure levels (*ta*), precipitation (*pr*), and surface pressure (*ps*). A list of the selected GCMs is provided in Table 3.

Table 3. Summary of the twenty CMIP6 GCMs utilized in study II.

Model	Resolution (lat × lon)	Country
ACCESS-CM2	$1.25^\circ \times 1.875^\circ$	Australia
ACCESS-ESM1-5	$1.25^\circ \times 1.875^\circ$	Australia
CanESM5	$2.8^\circ \times 2.8^\circ$	Canada
CMCC-CM2-SR5	$0.9375^\circ \times 1.25^\circ$	Italy
CMCC-ESM2	$0.9375^\circ \times 1.25^\circ$	Italy
EC-Earth3	$0.7^\circ \times 0.7^\circ$	The Netherlands/Ireland
FGOALS-g3	$2.25^\circ \times 2.0^\circ$	China
HadGEM3-GC31-LL	$1.25^\circ \times 1.875^\circ$	The UK
IPSL-CM6A-LR	$1.25^\circ \times 2.5^\circ$	France
KACE-1-0-G	$1.25^\circ \times 1.875^\circ$	South Korea
MIROC6	$1.4^\circ \times 1.4^\circ$	Japan
MIROC6-ES2L	$2.8125^\circ \times 2.8125^\circ$	Japan
MPI-ESM1-2-LR	$1.875^\circ \times 1.875^\circ$	Germany
MPI-ESM1-2-HR	$0.9375^\circ \times 0.9375^\circ$	Germany
MRI-ESM2-0	$1.125^\circ \times 1.125^\circ$	Japan
NESM3	$1.9^\circ \times 1.9^\circ$	China
NorESM2-LM	$1.875^\circ \times 2.5^\circ$	Norway
NorESM2-MM	$0.9375^\circ \times 0.9375^\circ$	Norway
TaiESM1	$0.9375^\circ \times 1.25^\circ$	Taiwan
UKESM1-0-LL	$1.25^\circ \times 1.875^\circ$	The UK

3.2. Physical Diagnostic Model

We use physical diagnostic model introduced by O’Gorman and Schneider (2009) to separate the *TH* and *DY* component from *Rx1Day*. The intensity of extreme precipitation (P_e) can be reproduced by the following equation:

$$P_e = - \left\{ \omega_e \frac{dq_s}{dp} \Big|_{\theta^*} \right\} \quad \text{Eq. (7)}$$

Where $\{\cdot\} = \frac{1}{g} \int_{p_0}^p \cdot dp$, denotes the mass-weighted integral over the troposphere. ω_e represents the pressure vertical velocity, and $\frac{dq_s}{dp} \Big|_{\theta^*}$ is the vertical derivative of the saturation specific humidity, evaluated along a moist adiabatic lapse rate. The physical diagnostic model is applied using atmospheric conditions from the specific day on which *Rx1Day* occurs. *TH* contribution is computed using Equation (7), but with the vertical velocity ω_e replaced by its time-mean value over the entire time series at each grid point. *DY* contribution is then obtained as the residual between the full *Rx1Day* and the *TH* component.

Finally, the relative change of extreme precipitation for each projected year is obtained by:

$$\Delta P_{e,t} = \frac{P_{e,t} - P_{e,h}}{P_{e,h}} \times 100\% \quad \text{Eq. (7)}$$

Where $P_{e,h}$ is the average extreme precipitation over the historical period. $P_{e,t}$ is the extreme precipitation for the projected year t and $\Delta P_{e,t}$ is the changes in extreme precipitation for the year t with relative to historical period.

3.3. Uncertainty Decomposition Framework

We apply the uncertainty decomposition framework of HS09 to decompose the uncertainty in changes to $Rx1Day$ between the two periods. The HS09 method is implemented in the following steps:

1. The time series of changes relative to historical period from 2021-2100 for each model and each scenario are fitted to the fourth-order polynomials using ordinary least square method. The relative changes for each projected year can be expressed by:

$$\Delta P_{e,t} = x_{m,s,t} + \epsilon_{m,s,t} \quad \text{Eq. (8)}$$

Here, $x_{m,s,t}$ are the fitted value and $\epsilon_{m,s,t}$ is the residual of model m , scenario s and year t .

2. In each GCM, the internal variability is defined as the multi-model averaged variance of the residuals as shown below:

$$V_t = \frac{1}{N_m} \sum_m var_{s,t}(\epsilon_{m,s,t}) \quad \text{Eq. (9)}$$

Where $var_{s,t}(\epsilon_{m,s,t})$ is the variance of $\epsilon_{m,s,t}$ across the scenarios and year while N_m is the number of GCMs.

3. The model uncertainty is obtained from the multi-model mean of the fitted

values under each scenario as shown below:

$$M_t = \frac{1}{N_s} \sum_s var_s(x_{m,s,t}) \quad \text{Eq. (10)}$$

Where N_s is the number of scenarios.

4. The scenario uncertainty is the variance of multi-model mean of the fitted values under each scenario as shown below:

$$S_t = var_s \left(\frac{1}{N_m} \sum_m x_{m,s,t} \right) \quad \text{Eq. (11)}$$

5. The total uncertainty is obtained by:

$$T_t = V + M + S \quad \text{Eq. (12)}$$

6. The proportional contribution from each source is calculated as the fraction of its individual uncertainty (V, M, S) relative to the total uncertainty (T).

3.4. Signal-to-Noise Ratio (*SNR*)

SNR provides a measure of how uncertainty affects the climate change signal in the projections. In the HS09 framework, the fitted value is considered the true signal of climate change, while the total uncertainty computed from Equation (12) is treated as noise. Based on this, the *SNR* is calculated as:

$$SNR_t = \frac{\bar{x}_{*,*,t}}{1.65 \times \sqrt{T_t}} \quad \text{Eq. (13)}$$

Since the variable of interest is the change in extreme precipitation, the signal can be either positive (indicating an increase) or negative (indicating a decrease). In this

context, an *SNR* value between -1 and 1 implies that the noise is large relative to the signal, making the projection highly uncertain and thus unreliable. Conversely, when the *SNR* deviates significantly from zero, it indicates a clearer signal. This means that if the projection indicates an increase (or decrease), there is a higher likelihood that this change will occur, making the information more actionable for decision-makers.

4. Results

4.1. Changes of *Rx1Day* and the Contributions from *TH* and *DY*

To initiate our analysis, we first examine the spatial patterns and temporal trends in *Rx1Day* to identify regions prone to significant increases or decreases. Figures 16 (a), (c), and (e) show the spatial patterns of changes in *Rx1Day*, averaging over all simulation years and across all GCMs for the three emissions scenarios. Correspondingly, Figures 16 (b), (d), and (f) illustrate the temporal trends, averaged over all grid points and GCMs, and regressed against years. The spatial patterns indicate that, in the future, *Rx1Day* is projected to increase across most parts of the world, particularly overland areas where human populations are concentrated and where hydrological disasters such as floods, mudslides, and landslides are most likely to occur. This general pattern is consistent across all three emissions scenarios, though the magnitude of change varies. SSP1-2.6 shows the smallest changes, while SSP5-8.5 exhibits the most intense changes, both positive and negative. This suggests that without concerted efforts to mitigate emissions and regulate the pace of technological and economic growth, the risk of extreme precipitation events and associated natural

disasters will likely increase. Regions projected to experience the most significant increases in *Rx1Day* include equatorial land areas, especially central Africa, as well as the equatorial Pacific Ocean. In contrast, notable decreases are projected in the equatorial regions of the northern and southern Atlantic, as well as parts of the southern Pacific Ocean. Meanwhile, over time, *Rx1Day* exhibits considerable interannual variability in all three emissions scenarios, especially under the lower-emission pathways. In SSP1-2.6 and SSP2-4.5, no consistent increasing or decreasing trend is observed, with values fluctuating significantly from year to year. In contrast, SSP5-8.5 shows a clearer pattern, with a statistically significant upward trend emerging from the regression analysis. This suggests that only under high-emission conditions does *Rx1Day* show a sustained increase over time, while lower-emission scenarios are characterized by high variability without a clear directional change. From these insights, although *Rx1Day* generally shows an increasing trend in many regions, as expected under climate change, certain areas exhibit unexpectedly intense increases or decreases. Furthermore, when examining temporal changes, no consistent trend is observed—except under the high-emission scenario, SSP5-8.5, which shows a clear upward trajectory. These deviations from the expected patterns highlight the need to investigate the underlying drivers of variability. In particular, it is crucial to assess whether *TH* and *DY* factors can help explain these spatial and temporal variations in *Rx1Day* changes.

Figure 17 shows the separated *Rx1Day* into *TH* and *DY*, displayed spatially (a, d, g, b, e, h) and temporally (c, f, i) across the three emission scenarios. In every grid of *TH*, the changes are positive, indicating that *TH* consistently drives the expectation of

Rx1Day to increase over time. However, the intensity of this increase depends on the level of future emissions. In contrast, *DY* is the main driver of the direction of full change that was observed in Figure 16. The pattern of full changes largely follows the pattern of *DY*. Intense increases or decreases are primarily driven by *DY*. However, the spatial pattern of *DY* is chaotic, with both positive and negative changes scattered across regions, indicating high spatial variability and a more complex influence on *Rx1Day* trends. In areas where *DY* increases, the full change is intense. In contrast, in regions where *DY* declines, even with an increase in *TH*, the resulting full change is either minimal or slightly negative. Temporally, *TH* causes *Rx1Day* to increase steadily over the years, in line with the CC scaling. In all three emission scenarios, the *TH* trend is significantly increasing when regressed against years, with the highest rate of change observed under the high-emission scenario. On the other hand, *DY* exhibits chaotic temporal behavior. Its changes are unpredictable, with intensities swinging up and down from year to year. Sudden shifts from low to high values occur across all scenarios. These results help explain the findings in Figure 16—the chaotic nature of *Rx1Day* is primarily driven by *DY*, while *TH* increases steadily as expected based on thermodynamic principles.

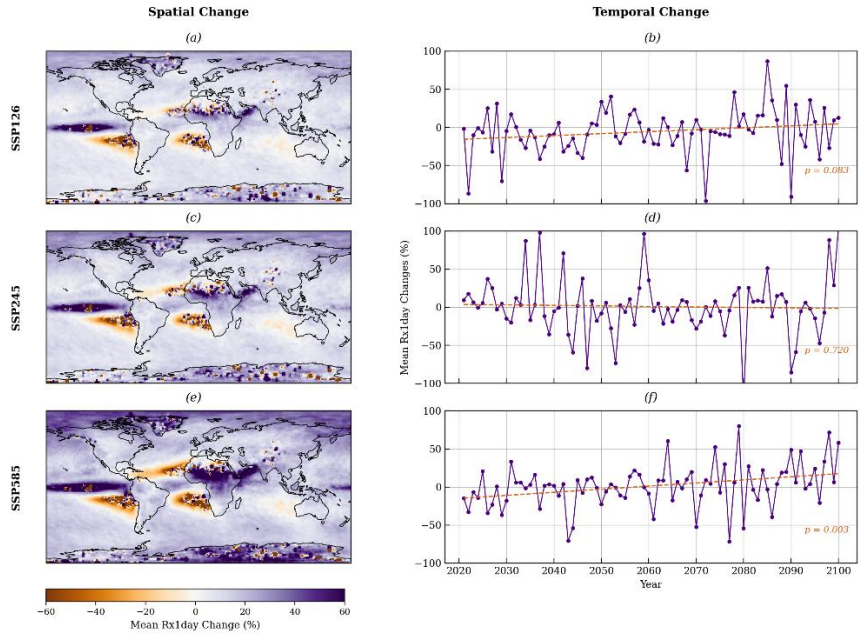


Figure 16. Spatial and temporal changes in **Rx1Day** under SSP1-2.6 (a, b), SSP2-4.5 (c, d), and SSP5-8.5 (e, f). Panels (a), (c), and (e) show spatial averages across all years and GCMs for each scenario at each grid point. Panels (b), (d), and (f) display temporal trends, computed as averages over all grids and GCMs for each scenario by year, followed by linear regression. The orange text indicates the p-value of the regression.

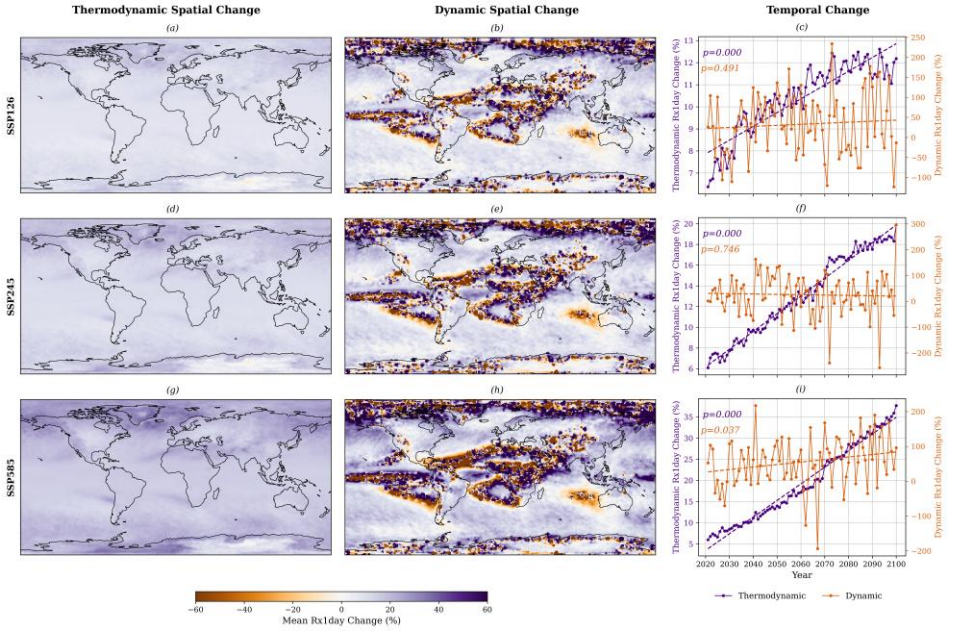


Figure 17. Spatial and temporal changes in ***TH*** and ***DY*** components under SSP1-2.6 (a, b, c), SSP2-4.5 (d, e, f), and SSP5-8.5 (g, h, i). Panels (a, d, g) and (b, e, h) show spatial averages across all years and GCMs for each scenario at each grid point for ***TH*** and ***DY*** respectively. Panels (c), (f), and (i) display temporal trends, computed as averages over all grids and GCMs for each scenario by year, followed by linear regression. The left-y axis for ***TH*** represented purple while the right-y for ***DY*** represented orange color. The texts indicate the p-value of the regression.

4.2. Uncertainty of Changes and the Decomposition

We now examine the uncertainty in projected changes in *Rx1Day*, *TH*, and *DY* components, decomposed into internal variability, model uncertainty, and scenario uncertainty. In Figure 18, panels (a), (c), and (e) show the percentage contributions from each uncertainty source, while panels (b), (d), and (f) present the absolute magnitude of total uncertainty over time. Uncertainty in *Rx1Day* increases throughout the 21st century, largely driven by rising model and scenario contributions. For the *TH*

component, uncertainty begins at a low level dominated by internal variability but grows after the 2040s as model and scenario influences become more prominent. Nevertheless, TH uncertainty remains relatively small compared to DY . The DY component exhibits consistently high uncertainty across the entire period, with internal variability being the dominant source. Scenario contributions to DY are negligible, and model contributions remain below 10% throughout. This pattern explains the decomposition of $Rx1Day$ uncertainty in panel (a), where internal variability is the largest contributor, primarily reflecting DY . After around mid-century, the increasing role of model and scenario uncertainty—mostly stemming from TH . Overall, internal variability is mainly associated with DY , while the model and scenario uncertainties that emerge later are largely attributed to TH .

Next, we investigate the spatial contributions of the three sources of uncertainty. As shown in previous results, the relative contributions—particularly for the TH component—evolve over time. To capture this temporal variation, we divide the projection period into three distinct time slices: 2021–2040 (near future), 2051–2070 (mid future), and 2081–2100 (far future). Figure 19 shows that internal variability is the dominant source of uncertainty in projected changes, especially in the Near and Mid Future. For changes in $Rx1Day$, internal variability accounts for more than 90% of the total uncertainty in these early periods. However, in the Far Future, its influence declines, particularly in regions where intense changes were previously observed (Figures 16 and 17). This decline is primarily due to increased contributions from both

model and scenario uncertainties. Notably, these increases are more prominent in tropical regions such as Central Africa and the Equatorial Pacific Ocean—areas characterized by complex large-scale circulation patterns that are challenging for GCMs to simulate accurately, thereby increasing model uncertainty. Examining the individual components, the *DY* contribution is dominated by internal variability across most regions and time slices. However, in the Far Future, model uncertainty becomes more prominent in certain areas, including Central Africa and the Brazilian Amazon. In contrast, for the *TH* component, internal variability dominates in the near future, but significant changes are observed in the mid future. In tropical regions, internal variability decreases markedly as both model and scenario contributions increase—particularly the latter, due to varying emission pathways. This is expected, as tropical regions receive high solar radiation and are highly sensitive to temperature increases, which are closely linked to emissions. Consequently, scenario uncertainty plays a more significant role in shaping the thermodynamic response in these areas. By the Far Future, the influence of internal variability on *TH* becomes minimal compared to earlier periods, while scenario uncertainty emerges as the dominant contributor on a global scale.

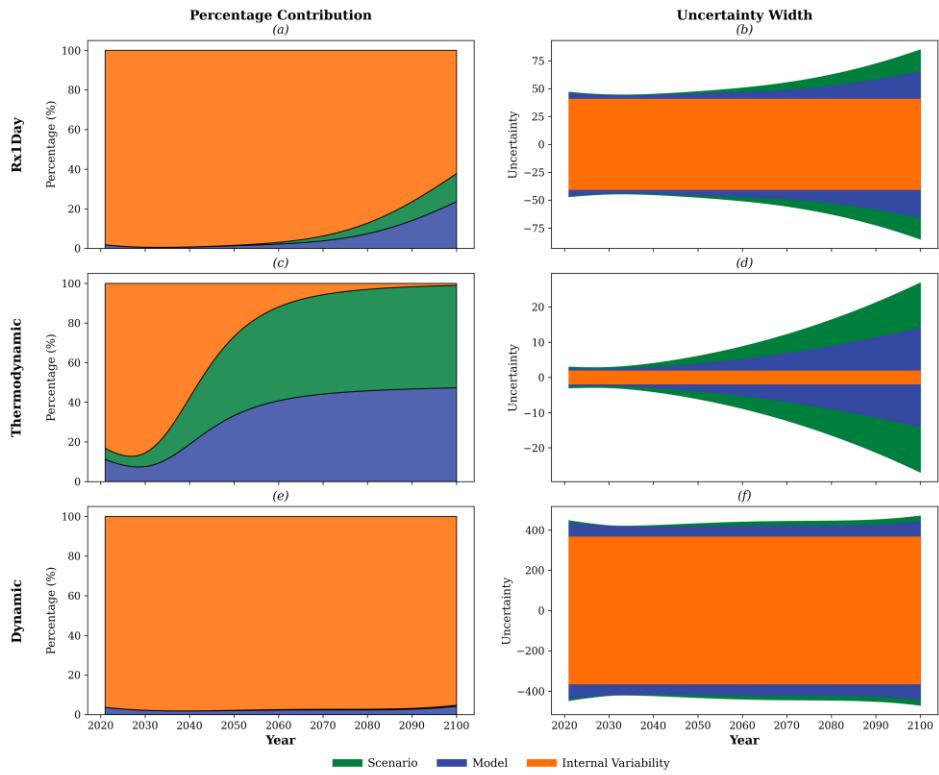


Figure 18. Uncertainty contributions from the three sources for the global average over time (a, c, e), and the corresponding total uncertainties (b, d, f). Panels (a, b) represent **Rx1Day** changes, (c, d) show its **TH** component, and (e, f) illustrate the **DY** component.

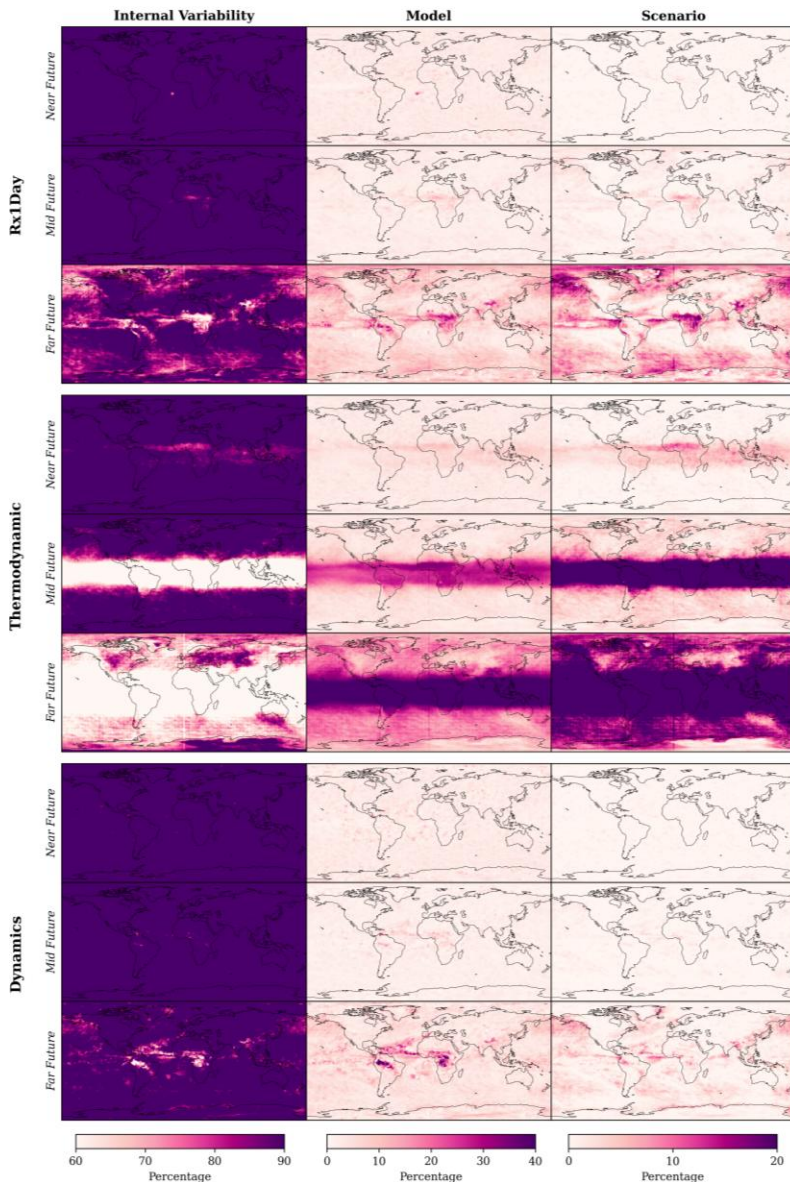


Figure 19. Global uncertainty contributions from all sources. Each large panel represents **Rx1Day** changes (first), **TH** (second), and **DY** (last). Each column corresponds to a different source of uncertainty, and each row shows a different time slice: Near Future (2021–2040), Mid Future (2051–2070), and Far Future (2081–2100).

4.3. *SNR* Analysis

Following the previous analysis, we conducted an *SNR* assessment to evaluate how uncertainty affects the evolving signals of the *TH* and *DY* components, and how noise within each contributes to the overall change in *Rx1Day*. Figure 20 illustrates the *SNR* of *TH* and *DY* across the three time slices described earlier. The results show that the signal from *TH* is relatively strong, particularly in tropical regions, indicating low associated uncertainty. This implies that projections driven by *TH* are more robust in these regions. In contrast, the mid- to high-latitude regions exhibit low *SNR*, meaning that noise outweighs the signal, rendering projections less reliable. When comparing the three time periods, we observe that *SNR* in the near future is relatively high but declines over time. This trend is driven by an increase in noise, as also shown in Figure 18. On the other hand, *DY* exhibits consistently low *SNR* across all regions and time periods, indicating that its signal is very weak relative to the noise. This suggests that projections based on *DY* are highly uncertain and chaotic, making it difficult to rely on them for future planning.

Next, we examine how noise from the *TH* and *DY* components influence the signal of changes in *Rx1Day*, as shown in Figure 21. The results indicate that noise from *TH* has a minimal impact on the *Rx1Day* signal, especially in regions experiencing intense changes—primarily near the equator over both ocean and land areas. Even in areas with negative changes, the signal remains strong relative to *TH* noise, suggesting that

uncertainty from the *TH* contributes little to the overall *Rx1Day* change signal. In contrast, noise from *DY* substantially affects the *Rx1Day* signal. Only in regions of intense change does the *SNR* exceed values of ± 1 , indicating a stronger signal relative to noise. Elsewhere, the *SNR* hovers near zero, implying that noise from the *DY* component dominates and makes the *Rx1Day* projections less reliable. When comparing across years, no significant differences are observed—particularly for *DY*, which consistently exerts a similar influence on the *Rx1Day* change signal throughout the period.

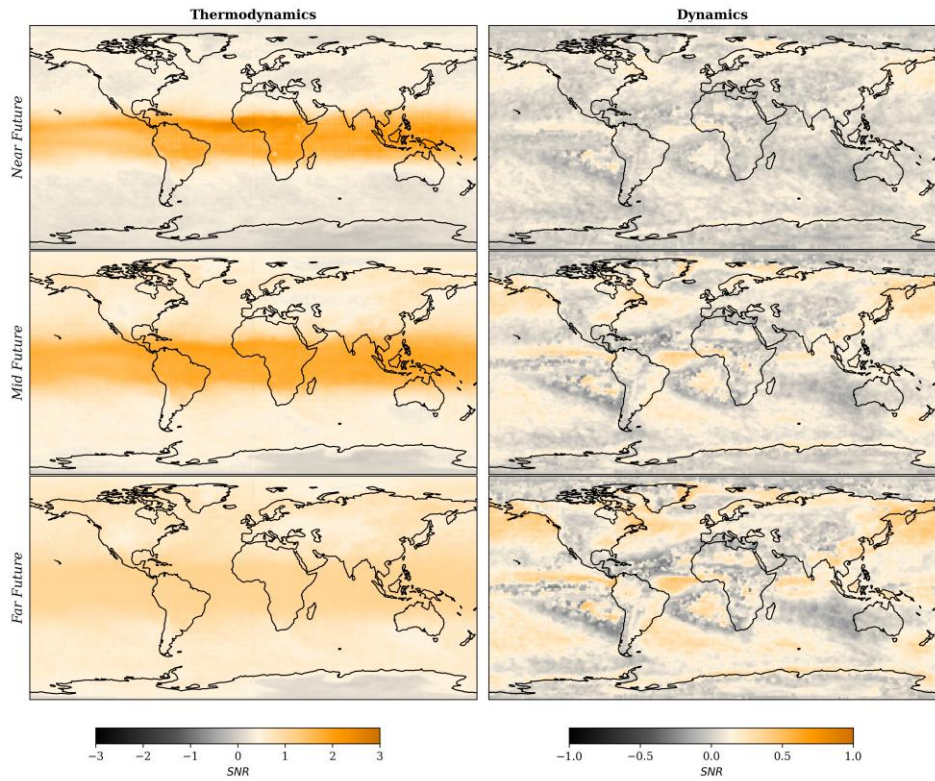


Figure 20. Spatially distribution of SNR for **TH** (first column) and **DY** (second column). Each row shows a different time slice: Near Future (2021–2040), Mid Future (2051–2070), and Far Future (2081–2100).

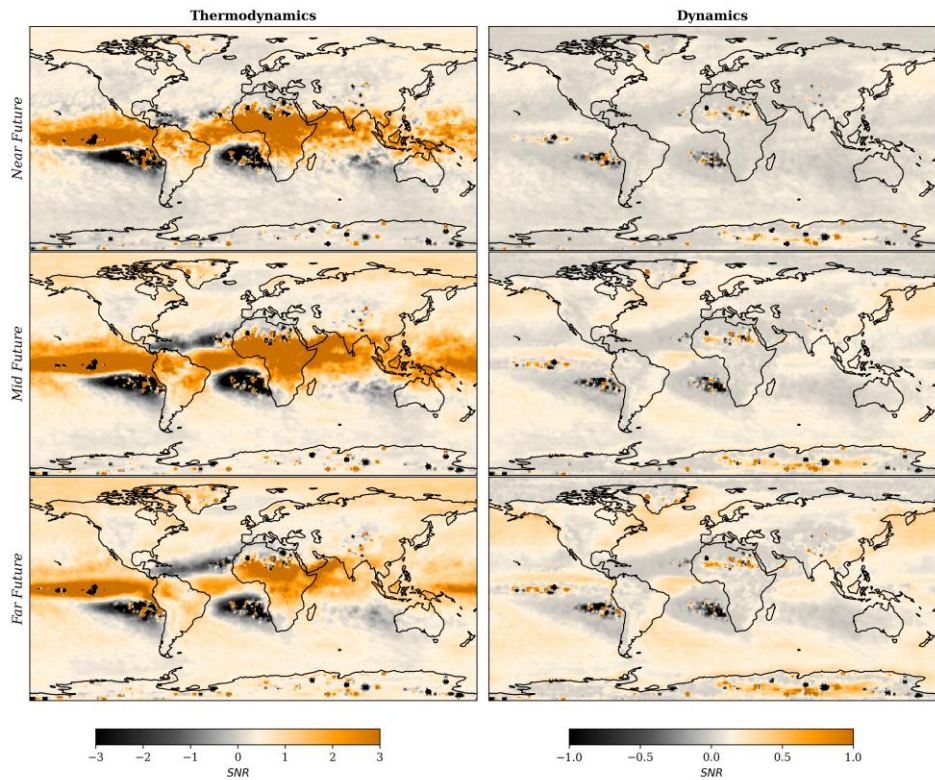


Figure 21. Spatially distribution of how noise in **TH** (first column) and **DY** (second column) would affect the signal of **Rx1Day** changes. Each row shows a different time slice: Near Future (2021–2040), Mid Future (2051–2070), and Far Future (2081–2100).

5. Discussions

Climate projections are essential for informing policy decisions, particularly in guiding preparation and mitigation strategies. This study contributes to the field by investigating the sources of uncertainty in extreme precipitation changes, with a focus on both *DY* and *TH* components. Previous studies (e.g., Lafferty and Sriver, 2023; Zhang and Chen, 2021) have consistently found that internal variability is the dominant contributor to uncertainty, especially at the beginning of the projection period. Building on these findings, our study aims to explore the underlying physical mechanisms driving these uncertainties by decomposing extreme precipitation into its two primary components *TH* and *DY*—using the physical diagnostic model introduced by O’Gorman and Schneider (2009).

Consistent with earlier studies (Dai and Nie, 2021; Li et al., 2025; Ritzhaupt and Maraun, 2024), we find that *TH* contributes to a near-linear increase in extreme precipitation over time. This trend arises because *TH* is closely linked to temperature, and as global temperatures rise (Gu et al., 2023), the atmosphere can hold more moisture, intensifying precipitation. However, the global signal associated with *TH* is relatively small compared to that from *DY*, which reflects changes in atmospheric circulation at both small and large scales. *DY* plays a critical role in determining the regional patterns of extreme precipitation change. Our results show that tropical and equatorial regions are particularly susceptible to strong changes in *DY*, leading to more intense extreme precipitation events in these areas. The increase or decrease in the *DY*

component is primarily driven by the inherently chaotic nature of the Earth's climate system. Under changing climate conditions, previous studies have shown that large-scale atmospheric circulation patterns are projected to shift in some regions (Ma and Yu, 2014; Plesca et al., 2018). These shifts in circulation patterns significantly influence extreme precipitation by either amplifying or suppressing it, depending on the region and the direction of change in the dynamic processes (Horton et al., 2015).

By decomposing the uncertainty in both *TH* and *DY* components, we are able to address the core questions posed in this study. The substantial contribution of internal variability to extreme precipitation uncertainty, as found in previous studies, is primarily driven by the dynamical processes. Internal variability arises from the natural fluctuations of the Earth's system, which are closely linked to both large- and small-scale atmospheric circulation patterns (Horton et al., 2015). As a result, it accounts for over 90% of the uncertainty in the *DY* component. In the case of *TH*, internal variability also plays a dominant role at the beginning of the projection period, when scenario and model uncertainties are minimal. However, as time progresses, the influence of internal variability on *TH* diminishes, while uncertainties stemming from emission scenarios and models become increasingly significant. When combining the uncertainty contributions from both components, internal variability emerges as the dominant factor influencing the total uncertainty in extreme precipitation changes—particularly in the early stages of the projection. In the longer term, scenario-related uncertainty becomes more prominent for the *TH* component. Spatially, regions near

the equator, especially those with strong solar radiation and higher projected temperature increases, exhibit greater uncertainty in *TH* due to differences among emission scenarios and climate models. These regions are expected to experience larger temperature increases (IPCC, 2021), amplifying the divergence between high and low emission pathways and thus elevating scenario-related uncertainty. In contrast, for the *DY* component, internal variability remains the primary contributor to uncertainty globally. Scenario uncertainty has negligible influence on *DY*, while model uncertainty plays a more significant role in regions where large dynamical changes are projected, indicating substantial model disagreement in those areas.

Building on the uncertainty decomposition, we further explored how this uncertainty influences the signal of changes in both *TH* and *DY*, and how noise in each component may obscure the signal of *Rx1Day*. Interestingly, *SNR* behaves quite differently between the two. For *TH*, especially in equatorial regions—indicating that the signal is much the *SNR* is generally high—stronger than the noise. This suggests that in these regions, projections related to *TH* changes are more reliable. It has important implications for policymaking: since *TH* is expected to increase with rising temperatures, and the associated signal is relatively robust, it is likely that extreme precipitation will also intensify in these areas. This points to an elevated risk of climate-related hazards such as floods, landslides, and mudslides. What makes this particularly concerning is that many of these tropical regions—such as Brazil, Central Africa, India, and much of Southeast Asia—are densely populated and home to over half of the global

population (Lenton et al., 2023). Therefore, policymakers in these regions should be especially attentive to future projections and consider proactive adaptation and mitigation strategies. In contrast, the situation is more complex with *DY*. Here, the noise tends to be much higher, resulting in *SNR* values that are close to zero across many regions. This implies that the *DY* component of projected changes in extreme precipitation is highly uncertain and less reliable. For climate scientists and model developers, this presents an important challenge: reducing the uncertainty in *DY* is crucial if we are to improve the reliability of future projections. Understanding and constraining the sources of *DY* uncertainty, especially those tied to internal variability could be a key direction for future research and model development.

6. Conclusions of Study II

In this study, we assessed the uncertainty in projected changes of *Rx1Day* and further investigated its two underlying components: *TH* and *DY* processes. We decomposed the uncertainty into three main sources: climate models, emission scenarios, and internal variability. The separation of *TH* and *DY* from *Rx1Day* was performed using a physical diagnostic model, and relative changes were calculated between two periods: the historical baseline (1971–2000) and the future projection period (2021–2100). For this analysis, we used output from 20 GCMs from CMIP6 under three emission scenarios: SSP1-2.6, SSP2-4.5, and SSP5-8.5. To quantify the contributions of each uncertainty source, we adopted the method introduced in HS09, which involves fitting

the model outputs to a fourth-order polynomial, with the residuals interpreted as internal variability.

By conducting both spatial and temporal analyses at the global scale, several meaningful findings have emerged. First, we found that *Rx1Day* is projected to increase in the future, particularly over global land areas, with the intensity of change increasing alongside emission levels. However, certain regions are expected to experience disproportionately high rates of increase, as well as regions with relatively low or even negative changes. This spatial heterogeneity can largely be attributed to the *DY* component, which modulates the expected warming-driven increase in *Rx1Day*. In contrast, the *TH* component showed a globally consistent, linear increase throughout the century, reflecting its dependence on rising temperatures. When evaluating uncertainty, we found that the *DY* component exhibits substantial uncertainty from the beginning of the projection period, whereas uncertainty in the *TH* component increases over time, largely driven by divergence among models and emission scenarios. Upon decomposing the sources of uncertainty, internal variability emerged as the dominant contributor to the overall uncertainty in *Rx1Day* changes. Further examination of *TH* and *DY* reveals that internal variability is primarily associated with *DY*, accounting for more than 90% of its uncertainty throughout the century. Meanwhile, model and scenario uncertainty in *Rx1Day* projections are largely attributable to the *TH* component, especially after the mid-century. Lastly, we evaluated the *SNR* of both *TH* and *DY* to assess the reliability of their projected signals.

The noise in *TH* was found to be relatively small compared to its signal, resulting in a high *SNR* and thus supporting the robustness of projections based on *TH*. This is particularly evident in tropical regions near the equator, where strong signals suggest a future increase in extreme precipitation. In contrast, the *DY* component is characterized by a low *SNR* due to its high noise, rendering its signal less trustworthy. This reflects the chaotic nature of atmospheric dynamics and highlights the challenge of predicting future circulation changes. Moreover, when assessing the influence of noise from each component on the overall *Rx1Day* signal, we found that *TH* noise has only a minimal impact, while *DY* noise substantially degrades the signal, reducing the reliability of *Rx1Day* projections in many regions.

V. Overall Conclusions

In this thesis, we assessed two important perspectives of extreme precipitation: (1) how extreme precipitation scales with temperature (scaling rates), and (2) its actual changes between the historical and projected future periods. A central focus was placed on the uncertainty of these projections and their decomposition into different sources. We believe these findings contribute meaningfully to both academic research and practical applications for policymakers.

In the first study, we found that the choice of GCMs is the dominant contributor to uncertainty in scaling rates across many regions. This suggests that future research should prioritize careful selection of climate models rather than allocating significant effort to including multiple emission scenarios, as scenario-related uncertainty was comparatively small in most regions. However, in areas where the choice of scaling method contributes more to overall uncertainty, applying a variety of scaling techniques could help capture a broader range of possible outcomes. A key outcome of this analysis is the identification of the minimum number of GCMs required to obtain a robust estimate: we found that using only 9 GCMs is sufficient for most regions. This insight is particularly valuable, as using a large number of models can be computationally expensive. However, regional differences still exist, so researchers should consider the specific characteristics of their study area before generalizing this number. Additionally, for researchers debating whether to use CMIP5 or CMIP6

models, our results offer some guidance. While both ensembles produce similar global averages, regional differences do exist. Notably, we found that GCMs uncertainty tends to be lower in CMIP6 compared to CMIP5, suggesting that model improvements in CMIP6 have contributed to a reduction in uncertainty spread. This supports the idea that CMIP6 models may offer more reliable projections in many cases.

In the second study, we focused on the actual changes in *Rx1Day* between the historical and future projection periods. To better understand the drivers of uncertainty in these changes, we decomposed the total uncertainty into three major sources: climate model uncertainty, emission scenario uncertainty, and internal variability. Furthermore, we separated *Rx1Day* changes into their *DY* and *TH* components using a physical diagnostic model. Our global assessment revealed a general increase in *Rx1Day*, particularly across land areas where human populations are concentrated. However, we also identified certain regions experiencing either unusually intense increases or even localized decreases. These contrasting patterns are better explained when *Rx1Day* is separated into its *TH* and *DY* components. *TH* exhibits a clear global upward trend, aligned with the expected response to rising temperatures. In contrast, *DY* introduces significant regional variability—sometimes amplifying and sometimes suppressing the overall *Rx1Day* signal. In many regions, the magnitude of *DY* dominates the signal, making *Rx1Day* changes more reflective of dynamic shifts than thermodynamic trends. Importantly, *DY* is associated with substantial uncertainty throughout the entire projection period, with internal variability as the dominant source. Meanwhile, *TH*

uncertainty grows over time, as model structure and emission scenarios begin to diverge more significantly, especially after the mid-century. From an application perspective, this has meaningful implications. We evaluated the *SNR* of both *DY* and *TH*, which helps determine how reliable the projected changes are relative to their uncertainty. The *SNR* for *TH* was found to be high, especially in tropical regions, indicating that the *TH* component of *Rx1Day* can serve as a relatively robust basis for future planning. This is crucial for policymakers in regions such as Southeast Asia, Central Africa, and parts of South America, where high *SNR* coincides with high exposure to climate impacts. Conversely, the *DY* component was characterized by a very low *SNR*, reflecting high uncertainty and low confidence in regional projections. This poses a significant challenge for local-scale adaptation planning. To improve the utility of future projections, climate modelers must focus on better representing local and large-scale circulation patterns that drive the *DY* component. Additionally, given the large uncertainty involved, strategies such as emergent constraints or probabilistic frameworks could be instrumental in narrowing uncertainty and making future projections more actionable.

In summary, for policymakers and planners aiming to prepare for future extremes, these findings underscore the importance of considering both components of change—not just the trend, but also the variability and uncertainty. Integrating uncertainty quantification into climate risk assessments is not just a scientific necessity, but a practical step toward more resilient infrastructure and disaster preparedness strategies.

References

- Abbe, C., 1901. THE PHYSICAL BASIS OF LONG-RANGE WEATHER FORECASTS1.
- Aldardasawi, A.F.M., Eren, B., 2021. Floods and Their Impact on the Environment. *Acad. Perspect. Procedia* 4, 42–49. <https://doi.org/10.33793/acperpro.04.02.24>
- Alduchov, O.A., Eskridge, R.E., 1996. Improved Magnus Form Approximation of Saturated Vapor Pressure.
- Ali, H., Fowler, H.J., Mishra, V., 2018. Global Observational Evidence of Strong Linkage Between Dew Point Temperature and Precipitation Extremes. *Geophys. Res. Lett.* 45, 12,320-12,330. <https://doi.org/10.1029/2018GL080557>
- Ali, H., Fowler, H.J., Pritchard, D., Lenderink, G., Blenkinsop, S., Lewis, E., 2022. Towards Quantifying the Uncertainty in Estimating Observed Scaling Rates. *Geophys. Res. Lett.* 49, e2022GL099138. <https://doi.org/10.1029/2022GL099138>
- Allan, R.P., Soden, B.J., 2008. Atmospheric Warming and the Amplification of Precipitation Extremes. *Science* 321, 1481–1484. <https://doi.org/10.1126/science.1160787>
- Allen, M.R., Ingram, W.J., 2002. Constraints on future changes in climate and the hydrologic cycle. *Nature* 419, 224–232. <https://doi.org/10.1038/nature01092>
- Archer, G.E.B., Saltelli, A., Sobol, I.M., 1997. Sensitivity measures,anova-like Techniques and the use of bootstrap. *J. Stat. Comput. Simul.* 58, 99–120. <https://doi.org/10.1080/00949659708811825>
- Blanusa, M.L., López-Zurita, C.J., Rasp, S., 2023. Internal variability plays a dominant role in global climate projections of temperature and precipitation extremes. *Clim. Dyn.* 61, 1931–1945. <https://doi.org/10.1007/s00382-023-06664-3>
- Braun, M., Thiombiano, A.N., Vieira, M.J.F., Stadnyk, T.A., 2021. Representing climate evolution in ensembles of GCM simulations for the Hudson Bay System. *Elem. Sci. Anthr.* 9, 00011. <https://doi.org/10.1525/elementa.2021.00011>
- Charney, J.G., Fjörtoft, R., Neumann, J. von, 1950. Numerical Integration of the Barotropic Vorticity Equation. *Tellus Dyn. Meteorol. Oceanogr.* 2. <https://doi.org/10.3402/tellusa.v2i4.8607>
- Chen, C.-A., Hsu, H.-H., Liang, H.-C., 2021. Evaluation and comparison of CMIP6 and CMIP5 model performance in simulating the seasonal extreme precipitation in the Western North Pacific and East Asia. *Weather Clim. Extrem.* 31, 100303. <https://doi.org/10.1016/j.wace.2021.100303>
- Clapeyron, E., 1834. Mémoire sur la puissance motrice de la chaleur. L' Ecole Polytech. XIV, 153–191.
- Clausius, R., 1850. Ueber die bewegende Kraft der Wärme und die Gesetze, welche

- sich daraus für die Wärmelehre selbst ableiten lassen. *Ann. Phys.* 155, 368–397. <https://doi.org/10.1002/andp.18501550306>
- Cleveland, W.S., 1979. Robust Locally Weighted Regression and Smoothing Scatterplots. *J. Am. Stat. Assoc.* 74, 829–836. <https://doi.org/10.1080/01621459.1979.10481038>
- Courant, R., Friedrichs, K., Lewy, H., 1928. Über die partiellen Differenzengleichungen der mathematischen Physik. *Math. Ann.* 100, 32–74. <https://doi.org/10.1007/BF01448839>
- Dai, P., Nie, J., 2021. What Controls the Interannual Variability of Extreme Precipitation? *Geophys. Res. Lett.* 48, e2021GL095503. <https://doi.org/10.1029/2021GL095503>
- Dai, P., Nie, J., Yu, Y., Wu, R., 2024. Constraints on regional projections of mean and extreme precipitation under warming. *Proc. Natl. Acad. Sci.* 121, e2312400121. <https://doi.org/10.1073/pnas.2312400121>
- Emori, S., Brown, S.J., 2005. Dynamic and thermodynamic changes in mean and extreme precipitation under changed climate. *Geophys. Res. Lett.* 32. <https://doi.org/10.1029/2005GL023272>
- Eom, J., Moss, R., Edmonds, J., Calvin, K., Clarke, L., Dooley, J., Kim, S.H., Kopp, R.E., Kyle, P., Luckow, P., Patel, P., Thomson, A., Wise, M., Zhou, Y., 2013. Scenarios of future socio-economics, energy, land use, and radiative forcing, in: *Engineering Response to Climate Change*, Second Edition. CRC Press, pp. 81–138. <https://doi.org/10.1201/b14051>
- Eyring, V., Bony, S., Meehl, G.A., Senior, C.A., Stevens, B., Stouffer, R.J., Taylor, K.E., 2016. Overview of the Coupled Model Intercomparison Project Phase 6 (CMIP6) experimental design and organization. *Geosci. Model Dev.* 9, 1937–1958. <https://doi.org/10.5194/gmd-9-1937-2016>
- Fischer, E.M., Knutti, R., 2016. Observed heavy precipitation increase confirms theory and early models. *Nat. Clim. Change* 6, 986–991. <https://doi.org/10.1038/nclimate3110>
- Fowler, H.J., Lentink, G., Prein, A.F., Westra, S., Allan, R.P., Ban, N., Barbero, R., Berg, P., Blenkinsop, S., Do, H.X., Guerreiro, S., Haerter, J.O., Kendon, E.J., Lewis, E., Schaer, C., Sharma, A., Villarini, G., Wasko, C., Zhang, X., 2021. Anthropogenic intensification of short-duration rainfall extremes. *Nat. Rev. Earth Environ.* 2, 107–122. <https://doi.org/10.1038/s43017-020-00128-6>
- Garg, S., Mishra, V., 2019. Role of Extreme Precipitation and Initial Hydrologic Conditions on Floods in Godavari River Basin, India. *Water Resour. Res.* 55, 9191–9210. <https://doi.org/10.1029/2019WR025863>
- Ghausi, S.A., Zehe, E., Ghosh, S., Tian, Y., Kleidon, A., 2024. Thermodynamically inconsistent extreme precipitation sensitivities across continents driven by cloud-radiative effects. *Nat. Commun.* 15, 10669. <https://doi.org/10.1038/s41467-024-55143-8>
- Green, A.C., Fowler, H.J., Blenkinsop, S., Davies, P.A., 2025. Precipitation extremes in 2024. *Nat. Rev. Earth Environ.* 6, 243–245. <https://doi.org/10.1038/s43017-024-55143-8>

025-00666-x

- Gu, L., Yin, J., Gentine, P., Wang, H.-M., Slater, L.J., Sullivan, S.C., Chen, J., Zscheischler, J., Guo, S., 2023. Large anomalies in future extreme precipitation sensitivity driven by atmospheric dynamics. *Nat. Commun.* 14, 3197. <https://doi.org/10.1038/s41467-023-39039-7>
- Hardwick Jones, R., Westra, S., Sharma, A., 2010. Observed relationships between extreme sub-daily precipitation, surface temperature, and relative humidity. *Geophys. Res. Lett.* 37. <https://doi.org/10.1029/2010GL045081>
- Hawkins, E., Sutton, R., 2009. The Potential to Narrow Uncertainty in Regional Climate Predictions. *Bull. Am. Meteorol. Soc.* 90, 1095–1108. <https://doi.org/10.1175/2009BAMS2607.1>
- Horton, D.E., Johnson, N.C., Singh, D., Swain, D.L., Rajaratnam, B., Diffenbaugh, N.S., 2015. Contribution of changes in atmospheric circulation patterns to extreme temperature trends. *Nature* 522, 465–469. <https://doi.org/10.1038/nature14550>
- Huang, Z., Tan, X., Gan, T.Y., Liu, B., Chen, X., 2023. Thermodynamically enhanced precipitation extremes due to counterbalancing influences of anthropogenic greenhouse gases and aerosols. *Nat. Water* 1, 614–625. <https://doi.org/10.1038/s44221-023-00107-3>
- IPCC, 2021. Climate Change 2021: The Physical Science Basis. Contribution of Working Group I to the Sixth Assessment Report of the Intergovernmental Panel on Climate Change, 1st ed. Cambridge University Press. <https://doi.org/10.1017/9781009157896>
- Jebeile, J., Crucifix, M., 2020. Multi-model ensembles in climate science: Mathematical structures and expert judgements. *Stud. Hist. Philos. Sci. Part A* 83, 44–52. <https://doi.org/10.1016/j.shpsa.2020.03.001>
- Ji, Y., Fu, J., Liu, B., Huang, Z., Tan, X., 2024. Uncertainty separation of drought projection in the 21st century using SMILEs and CMIP6. *J. Hydrol.* 628, 130497. <https://doi.org/10.1016/j.jhydrol.2023.130497>
- John, A., Douville, H., Ribes, A., Yiou, P., 2022. Quantifying CMIP6 model uncertainties in extreme precipitation projections. *Weather Clim. Extrem.* 36, 100435. <https://doi.org/10.1016/j.wace.2022.100435>
- Kharin, V.V., Zwiers, F.W., Zhang, X., Wehner, M., 2013. Changes in temperature and precipitation extremes in the CMIP5 ensemble. *Clim. Change* 119, 345–357. <https://doi.org/10.1007/s10584-013-0705-8>
- Knutti, R., Baumberger, C., Hirsch Hadorn, G., 2019. Uncertainty Quantification Using Multiple Models—Prospects and Challenges, in: Beisbart, C., Saam, N.J. (Eds.), *Computer Simulation Validation: Fundamental Concepts, Methodological Frameworks, and Philosophical Perspectives*. Springer International Publishing, Cham, pp. 835–855. https://doi.org/10.1007/978-3-319-70766-2_34
- Kuma, P., Bender, F.A.-M., Jönsson, A.R., 2023. Climate Model Code Genealogy and Its Relation to Climate Feedbacks and Sensitivity. *J. Adv. Model. Earth Syst.*

- 15, e2022MS003588. <https://doi.org/10.1029/2022MS003588>
- Lafferty, D.C., Srivatava, R.L., 2023. Downscaling and bias-correction contribute considerable uncertainty to local climate projections in CMIP6. *Npj Clim. Atmospheric Sci.* 6, 1–13. <https://doi.org/10.1038/s41612-023-00486-0>
- Lehner, F., Deser, C., Maher, N., Marotzke, J., Fischer, E.M., Brunner, L., Knutti, R., Hawkins, E., 2020. Partitioning climate projection uncertainty with multiple large ensembles and CMIP5/6. *Earth Syst. Dyn.* 11, 491–508. <https://doi.org/10.5194/esd-11-491-2020>
- Lenderink, G., Mok, H.Y., Lee, T.C., van Oldenborgh, G.J., 2011. Scaling and trends of hourly precipitation extremes in two different climate zones – Hong Kong and the Netherlands. *Hydrol. Earth Syst. Sci.* 15, 3033–3041. <https://doi.org/10.5194/hess-15-3033-2011>
- Lenderink, G., van Meijgaard, E., 2008. Increase in hourly precipitation extremes beyond expectations from temperature changes. *Nat. Geosci.* 1, 511–514. <https://doi.org/10.1038/ngeo262>
- Lenton, T.M., Xu, C., Abrams, J.F., Ghadiali, A., Loriani, S., Sakschewski, B., Zimm, C., Ebi, K.L., Dunn, R.R., Svenning, J.-C., Scheffer, M., 2023. Quantifying the human cost of global warming. *Nat. Sustain.* 6, 1237–1247. <https://doi.org/10.1038/s41893-023-01132-6>
- Li, C., Liu, J., Du, F., Zwiers, F.W., Feng, G., 2025. Increasing certainty in projected local extreme precipitation change. *Nat. Commun.* 16, 850. <https://doi.org/10.1038/s41467-025-56235-9>
- Li, C., Zwiers, F., Zhang, X., Li, G., Sun, Y., Wehner, M., 2021. Changes in Annual Extremes of Daily Temperature and Precipitation in CMIP6 Models. *J. Clim.* 34, 3441–3460. <https://doi.org/10.1175/JCLI-D-19-1013.1>
- Li, S.-Y., Miao, L.-J., Jiang, Z.-H., Wang, G.-J., Gnyawali, K.R., Zhang, J., Zhang, H., Fang, K., He, Y., Li, C., 2020. Projected drought conditions in Northwest China with CMIP6 models under combined SSPs and RCPs for 2015–2099. *Adv. Clim. Change Res., Including special topic on East Asian climate response to 1.5/2 °C global warming* 11, 210–217. <https://doi.org/10.1016/j.accre.2020.09.003>
- Liu, X., Köhl, A., Stammer, D., Masuda, S., Ishikawa, Y., Mochizuki, T., 2017. Impact of in-consistency between the climate model and its initial conditions on climate prediction. *Clim. Dyn.* 49, 1061–1075. <https://doi.org/10.1007/s00382-016-3194-4>
- Ma, J., Yu, J.-Y., 2014. Paradox in South Asian summer monsoon circulation change: Lower tropospheric strengthening and upper tropospheric weakening. *Geophys. Res. Lett.* 41, 2934–2940. <https://doi.org/10.1002/2014GL059891>
- Maher, N., Milinski, S., Ludwig, R., 2021. Large ensemble climate model simulations: introduction, overview, and future prospects for utilising multiple types of large ensemble. *Earth Syst. Dyn.* 12, 401–418. <https://doi.org/10.5194/esd-12-401-2021>
- Manabe, S., Möller, F., 1961. ON THE RADIATIVE EQUILIBRIUM AND HEAT

BALANCE OF THE ATMOSPHERE.

- Manabe, S., Strickler, R.F., 1964. Thermal Equilibrium of the Atmosphere with a Convective Adjustment. *J. Atmospheric Sci.* 21, 3–15. [https://doi.org/10.1175/1520-0469\(1964\)021<003:TEAOAT>2.0.CO;2](https://doi.org/10.1175/1520-0469(1964)021<003:TEAOAT>2.0.CO;2)
- Manabe, S., Wetherald, R.T., 1975. The Effects of Doubling the CO₂ Concentration on the climate of a General Circulation Model. *J. Atmospheric Sci.* 32, 3–15. [https://doi.org/10.1175/1520-0469\(1975\)032<003:TEODTC>2.0.CO;2](https://doi.org/10.1175/1520-0469(1975)032<003:TEODTC>2.0.CO;2)
- Manabe, S., Wetherald, R.T., 1967. Thermal Equilibrium of the Atmosphere with a Given Distribution of Relative Humidity.
- Martel, J.-L., Brissette, F., Troin, M., Arsenault, R., Chen, J., Su, T., Lucas-Picher, P., 2022. CMIP5 and CMIP6 Model Projection Comparison for Hydrological Impacts Over North America. *Geophys. Res. Lett.* 49, e2022GL098364. <https://doi.org/10.1029/2022GL098364>
- Martinkova, M., Kysely, J., 2020. Overview of Observed Clausius-Clapeyron Scaling of Extreme Precipitation in Midlatitudes. *Atmosphere* 11, 786. <https://doi.org/10.3390/atmos11080786>
- Matera, S., Borrelli, A., Bellucci, A., Alessandri, A., Pietro, P.D., Athanasiadis, P., Navarra, A., Gualdi, S., 2014. Impact of Atmosphere and Land Surface Initial Conditions on Seasonal Forecasts of Global Surface Temperature. <https://doi.org/10.1175/JCLI-D-14-00163.1>
- Miao, C., Wu, Y., Fan, X., Su, J., 2023. Projections of Global Land Runoff Changes and Their Uncertainty Characteristics During the 21st Century. *Earth's Future* 11, e2022EF003286. <https://doi.org/10.1029/2022EF003286>
- Mishra, V., Wallace, J.M., Lettenmaier, D.P., 2012. Relationship between hourly extreme precipitation and local air temperature in the United States. *Geophys. Res. Lett.* 39. <https://doi.org/10.1029/2012GL052790>
- Molnar, P., Fatichi, S., Gaál, L., Szolgay, J., Burlando, P., 2015. Storm type effects on super Clausius–Clapeyron scaling of intense rainstorm properties with air temperature. *Hydrol. Earth Syst. Sci.* 19, 1753–1766. <https://doi.org/10.5194/hess-19-1753-2015>
- Nakicenovic, N., Alcamo, J., Grubler, A., Riahi, K., Roehrl, R.A., Rogner, H.-H., Victor, N., 2000. Special Report on Emissions Scenarios (SRES), A Special Report of Working Group III of the Intergovernmental Panel on Climate Change. Cambridge University Press, Cambridge.
- O’Gorman, P.A., Schneider, T., 2009. The physical basis for increases in precipitation extremes in simulations of 21st-century climate change. *Proc. Natl. Acad. Sci.* 106, 14773–14777. <https://doi.org/10.1073/pnas.0907610106>
- O’Neill, B.C., Tebaldi, C., van Vuuren, D.P., Eyring, V., Friedlingstein, P., Hurtt, G., Knutti, R., Kriegler, E., Lamarque, J.-F., Lowe, J., Meehl, G.A., Moss, R., Riahi, K., Sanderson, B.M., 2016. The Scenario Model Intercomparison Project (ScenarioMIP) for CMIP6. *Geosci. Model Dev.* 9, 3461–3482. <https://doi.org/10.5194/gmd-9-3461-2016>
- Paik, S., An, S.-I., Min, S.-K., King, A.D., Kim, S.-K., 2023. Emergent constraints on future extreme precipitation intensification: from global to continental scales.

- Weather Clim. Extrem. 42, 100613.
<https://doi.org/10.1016/j.wace.2023.100613>
- Park, I.-H., Min, S.-K., 2017. Role of Convective Precipitation in the Relationship between Subdaily Extreme Precipitation and Temperature. *J. Clim.* 30, 9527–9537. <https://doi.org/10.1175/JCLI-D-17-0075.1>
- Paterson, D.L., Wright, H., Harris, P.N.A., 2018. Health Risks of Flood Disasters. *Clin. Infect. Dis.* 67, 1450–1454. <https://doi.org/10.1093/cid/ciy227>
- Pathak, R., Dasari, H.P., Ashok, K., Hoteit, I., 2023. Effects of multi-observations uncertainty and models similarity on climate change projections. *Npj Clim. Atmospheric Sci.* 6, 1–12. <https://doi.org/10.1038/s41612-023-00473-5>
- Pendergrass, A.G., Lehner, F., Sanderson, B.M., Xu, Y., 2015. Does extreme precipitation intensity depend on the emissions scenario? *Geophys. Res. Lett.* 42, 8767–8774. <https://doi.org/10.1002/2015GL065854>
- Pfahl, S., O’Gorman, P.A., Fischer, E.M., 2017. Understanding the regional pattern of projected future changes in extreme precipitation. *Nat. Clim. Change* 7, 423–427. <https://doi.org/10.1038/nclimate3287>
- Plesca, E., Grützun, V., Buehler, S.A., 2018. How Robust Is the Weakening of the Pacific Walker Circulation in CMIP5 Idealized Transient Climate Simulations? <https://doi.org/10.1175/JCLI-D-17-0151.1>
- Pumo, D., Carlino, G., Blenkinsop, S., Arnone, E., Fowler, H., Noto, L.V., 2019. Sensitivity of extreme rainfall to temperature in semi-arid Mediterranean regions. *Atmospheric Res.* 225, 30–44. <https://doi.org/10.1016/j.atmosres.2019.03.036>
- Raju, K.S., Kumar, D.N., 2020. Review of approaches for selection and ensembling of GCMs. *J. Water Clim. Change* 11, 577–599. <https://doi.org/10.2166/wcc.2020.128>
- Randall, D.A., Bitz, C.M., Danabasoglu, G., Denning, A.S., Gent, P.R., Gettelman, A., Griffies, S.M., Lynch, P., Morrison, H., Pincus, R., Thuburn, J., 2018. 100 Years of Earth System Model Development. <https://doi.org/10.1175/AMSMONOGRAPH-D-18-0018.1>
- Riahi, K., van Vuuren, D.P., Kriegler, E., Edmonds, J., O’Neill, B.C., Fujimori, S., Bauer, N., Calvin, K., Dellink, R., Fricko, O., Lutz, W., Popp, A., Cuartero, J.C., Kc, S., Leimbach, M., Jiang, L., Kram, T., Rao, S., Emmerling, J., Ebi, K., Hasegawa, T., Havlik, P., Humpenöder, F., Da Silva, L.A., Smith, S., Stehfest, E., Bosetti, V., Eom, J., Gernaat, D., Masui, T., Rogelj, J., Strefler, J., Drouet, L., Krey, V., Luderer, G., Harmsen, M., Takahashi, K., Baumstark, L., Doelman, J.C., Kainuma, M., Klimont, Z., Marangoni, G., Lotze-Campen, H., Obersteiner, M., Tabeau, A., Tavoni, M., 2017. The Shared Socioeconomic Pathways and their energy, land use, and greenhouse gas emissions implications: An overview. *Glob. Environ. Change* 42, 153–168. <https://doi.org/10.1016/j.gloenvcha.2016.05.009>
- Ritzhaupt, N., Maraun, D., 2024. State-of-the-art climate models reduce dominant dynamical uncertainty in projections of extreme precipitation. *Environ. Res.*

- Clim. 3, 021001. <https://doi.org/10.1088/2752-5295/ad2eb2>
- Saltelli, A., Annoni, P., Azzini, I., Campolongo, F., Ratto, M., Tarantola, S., 2010. Variance based sensitivity analysis of model output. Design and estimator for the total sensitivity index. Comput. Phys. Commun. 181, 259–270. <https://doi.org/10.1016/j.cpc.2009.09.018>
- Sansom, P.G., Stephenson, D.B., Ferro, C.A.T., Zappa, G., Shaffrey, L., 2013. Simple Uncertainty Frameworks for Selecting Weighting Schemes and Interpreting Multimodel Ensemble Climate Change Experiments. <https://doi.org/10.1175/JCLI-D-12-00462.1>
- Schroer, K., Kirchengast, G., 2018. Sensitivity of extreme precipitation to temperature: the variability of scaling factors from a regional to local perspective. Clim. Dyn. 50, 3981–3994. <https://doi.org/10.1007/s00382-017-3857-9>
- Seneviratne, S.I., Donat, M.G., Pitman, A.J., Knutti, R., Wilby, R.L., 2016. Allowable CO₂ emissions based on regional and impact-related climate targets. Nature 529, 477–483. <https://doi.org/10.1038/nature16542>
- Sobol', I.M., 1990. On sensitivity estimation for nonlinear mathematical models. Matem Mod 2, 112–118.
- Steinschneider, S., Herman, J.D., Kucharski, J., Abellera, M., Ruggiero, P., 2023. Uncertainty Decomposition to Understand the Influence of Water Systems Model Error in Climate Vulnerability Assessments. Water Resour. Res. 59, e2022WR032349. <https://doi.org/10.1029/2022WR032349>
- Strobach, E., Bel, G., 2017. The contribution of internal and model variabilities to the uncertainty in CMIP5 decadal climate predictions. Clim. Dyn. 49, 3221–3235. <https://doi.org/10.1007/s00382-016-3507-7>
- Sun, C., Liu, L., Li, L.-J., Wang, B., Zhang, C., Liu, Q., Li, R.-Z., 2018. Uncertainties in simulated El Niño–Southern Oscillation arising from internal climate variability. Atmospheric Sci. Lett. 19, e805. <https://doi.org/10.1002/asl.805>
- Taylor, K.E., Stouffer, R.J., Meehl, G.A., 2012. An Overview of CMIP5 and the Experiment Design. <https://doi.org/10.1175/BAMS-D-11-00094.1>
- Trenberth, K.E., Dai, A., Rasmusson, R.M., Parsons, D.B., 2003. The Changing Character of Precipitation. <https://doi.org/10.1175/BAMS-84-9-1205>
- Utsumi, N., Seto, S., Kanae, S., Maeda, E.E., Oki, T., 2011. Does higher surface temperature intensify extreme precipitation? Geophys. Res. Lett. 38. <https://doi.org/10.1029/2011GL048426>
- Van Dijk, A.I.J.M., Beck, H.E., Boergens, E., de Jeu, R.A.M., Dorigo, W.A., Edirisinghe, C., Forootan, E., Guo, E., Güntner, A., Hou, J., Mehrnegan, N., Mo, S., Preimesberger, W., Rahman, J., Rozas Larraondo, P., 2025. Global Water Monitor 2024, Summary Report.
- Wang, G., Sun, X., 2022. Monotonic Increase of Extreme Precipitation Intensity With Temperature When Controlled for Saturation Deficit. Geophys. Res. Lett. 49, e2022GL097881. <https://doi.org/10.1029/2022GL097881>
- Wang, H.-M., Chen, J., Xu, C.-Y., Zhang, J., Chen, H., 2020. A Framework to Quantify

- the Uncertainty Contribution of GCMs Over Multiple Sources in Hydrological Impacts of Climate Change. *Earths Future* 8, e2020EF001602. <https://doi.org/10.1029/2020EF001602>
- Wasko, C., Lu, W.T., Mehrotra, R., 2018. Relationship of extreme precipitation, dry-bulb temperature, and dew point temperature across Australia. *Environ. Res. Lett.* 13, 074031. <https://doi.org/10.1088/1748-9326/aad135>
- Wasko, C., Sharma, A., 2014. Quantile regression for investigating scaling of extreme precipitation with temperature. *Water Resour. Res.* 50, 3608–3614. <https://doi.org/10.1002/2013WR015194>
- Westra, S., Fowler, H.J., Evans, J.P., Alexander, L.V., Berg, P., Johnson, F., Kendon, E.J., Lenderink, G., Roberts, N.M., 2014. Future changes to the intensity and frequency of short-duration extreme rainfall. *Rev. Geophys.* 52, 522–555. <https://doi.org/10.1002/2014RG000464>
- Wu, Y., Miao, C., Slater, L., Fan, X., Chai, Y., Sorooshian, S., 2024. Hydrological Projections under CMIP5 and CMIP6: Sources and Magnitudes of Uncertainty. *Bull. Am. Meteorol. Soc.* 105, E59–E74. <https://doi.org/10.1175/BAMS-D-23-0104.1>
- Yip, S., Ferro, C.A.T., Stephenson, D.B., Hawkins, E., 2011. A Simple, Coherent Framework for Partitioning Uncertainty in Climate Predictions. *J. Clim.* 24, 4634–4643. <https://doi.org/10.1175/2011JCLI4085.1>
- Yoo, S., Ahn, K.-H., 2023. Understanding extreme precipitation scaling with temperature: insights from multi-spatiotemporal analysis in South Korea. *Environ. Res. Lett.* 18, 124032. <https://doi.org/10.1088/1748-9326/ad0afa>
- Zhang, S., Chen, J., 2021. Uncertainty in Projection of Climate Extremes: A Comparison of CMIP5 and CMIP6. *J. Meteorol. Res.* 35, 646–662. <https://doi.org/10.1007/s13351-021-1012-3>
- Zhang, S., Zhou, Z., Peng, P., Xu, C., 2023. A New Framework for Estimating and Decomposing the Uncertainty of Climate Projections. *J. Clim.* 37, 365–384. <https://doi.org/10.1175/JCLI-D-23-0064.1>

Abstract*

Quantifying Uncertainty in Future Extreme Precipitation
Projections: A Dual Focus on Scaling Rates and Physical Changes

MIN SOTHEARITH

*Department of Civil and Environmental Engineering
Graduate School, Kongju National University
Cheonan City, South Korea*

(Supervised by Professor Kuk-Hyun Ahn)

This thesis tackles the uncertainty in future projections of extreme precipitation, focusing on both scaling rates with temperature and the projected changes. The analysis of scaling rates across global land regions reveals that the dominant source of uncertainty is the GCMs, while future emission scenarios contribute relatively little. In some areas, the scaling method also plays a significant role. Notably, using around nine GCMs is sufficient to obtain robust estimates in most regions, and CMIP6 models tend to show lower GCMs' contribution to the uncertainty than CMIP5, reflecting possible improvements in model design. In terms of projected changes between the projection and historical periods, increases are evident globally, especially over densely populated

regions. Decomposing extreme precipitation into thermodynamic and dynamic components shows that thermodynamic changes are consistently positive and tightly linked to warming, while dynamic changes are highly variable across regions. Dynamic uncertainty is dominated by internal variability throughout the projection period, whereas thermodynamic uncertainty grows over time as the contribution of model and scenario increase. Signal-to-noise ratios indicate that the projected thermodynamic changes are relatively robust, particularly in the tropics, while dynamic components remain highly uncertain, limiting their utility for regional adaptation planning. These findings highlight the need to improve the representation of atmospheric dynamics in climate models and to integrate uncertainty quantification into climate risk assessments.

*A thesis submitted to the Committee of Graduate School, Kongju National University in partial fulfillment of the requirements for the Degree of Master of Science conferred in August 2025.

국문초록

미래 극한 강수 예측의 불확실성 정량화: 스케일링 속도와 물리적 변화에 대한 이중 관점

MIN SOTHEARITH

공주대학교 대학원 건설환경공학과

(지도교수: 안국현)

본 논문은 극한 강수의 미래 예측에서의 불확실성을 다루며, 온도에 따른 스케일링 비율과 예측 변화 모두에 초점을 맞춘다. 전 세계 육상 지역을 대상으로 한 스케일링 비율 분석 결과, 지배적인 불확실성의 원천은 일반순환모형(GCMs)이며, 미래 배출 시나리오는 상대적으로 작은 기여를 하는 것으로 나타났다. 일부 지역에서는 스케일링 방법 또한 중요한 역할을 한다. 특히 약 9 개의 GCM 을 사용하는 것으로 대부분의 지역에서 강건한 추정치를 얻기에 충분하며, CMIP6 모형은 CMIP5 에 비해 GCM 의 불확실성 기여가 낮게 나타나 모델 설계의 향상을 반영할 가능성이 있다. 예측 기간과 과거 기간 사이의 극한 강수 변화에 있어, 전 세계적으로 특히 인구 밀집 지역에서 증가가 뚜렷하게 나타난다. 극한 강수를 열역학적 성분과 역학적 성분으로 분해한 결과, 열역학적 변화는 일관되게 증가하는 경향을 보이며

온난화와 밀접하게 연관되어 있는 반면, 역학적 변화는 지역에 따라 매우 가변적이다. 예측 기간 전반에 걸쳐 역학적 불확실성은 내부 변동성에 의해 지배되며, 열역학적 불확실성은 모델 및 시나리오의 기여가 증가함에 따라 시간이 지남에 따라 커진다. 신호 대 잡음 비(signal-to-noise ratio)는 열역학적 변화가 특히 열대 지역에서 비교적 강건함을 시사하는 반면, 역학적 성분은 높은 불확실성을 유지하며 지역 적응 계획에서의 활용 가능성을 제한한다. 이러한 결과는 기후 모형에서 대기 역학의 표현을 개선할 필요성과 기후 위험 평가에 불확실성 정량화를 통합할 필요성을 강조한다.

Acknowledgment

I would like to express my deepest gratitude to my advisor and mentor, **Dr. Ahn Kuk-Hyun**, for his invaluable guidance from the very beginning. With little background in Earth science, I'm truly grateful for his support in helping me grow in this field.

Sincere thanks to everyone at **AHNLab** for their support since my first day in Korea. Special appreciation to **Victor**, **Davy**, and **Angelika** for helping me settle in, and to **Charles** for being a great seatmate and friend. I'm also thankful to **Kenneth** and **Hazel** for being part of this journey.

To my loved ones—thank you to my parents, **Mea Noun** and **Puk Ro**, for their sacrifices, and to my grandmother, **Yeay Nget**, for always standing by me. I honor my late grandfather, **Ta Phal**, who deeply inspired my academic path. I'm grateful to my uncles, **Pu Ra** and **Pu Ny**, for their steady guidance, and to **Bong Khourch**, for always checking in and supporting me. I'm especially thankful to **Povpov (Chanoun)**, whose constant support and belief in me have been a true source of strength throughout this journey.

MIN SOTHEARITH

June 2025